Pergamon

Geochimica et Cosmochimica Acta, Vol. 59, No. 16, pp. 3413–3444, 1995

0016-7037/95 $9.50 + .00

0016-7037(95)00214-6

Condensation of $CaO-MgO-Al_2O_3-SiO_2$ liquids from cosmic gases

SHIGEKAZU YONEDA[1,*] and LAWRENCE GROSSMAN[1,2]

[1]Department of the Geophysical Sciences, The University of Chicago, Chicago, IL 60637, USA
[2]Enrico Fermi Institute, The University of Chicago, Chicago, IL 60637, USA

(*Received December* 13, 1994; *accepted in revised form April* 27, 1995)

Abstract—The Berman (1983) activity-composition model for non-ideal liquid solutions in the $CaO-MgO-Al_2O_3-SiO_2$ (CMAS) system is incorporated into equilibrium condensation calculations which are used to explore the vapor-solid-liquid stability relations as a function of temperature and total pressure (P^{tot}) in a gas of solar composition, and as a function of temperature and dust/gas ratio at $P^{tot} = 1 \times 10^{-3}$ atm in gases produced by total vaporization of systems enriched in interstellar dust relative to the gas compared to solar abundances. Condensate liquids are very non-ideal, suggesting that results of previous attempts to model their formation using ideal solution models are highly inaccurate. As is the case for the Berman (1983) liquid model itself, results of the present calculations are in very good agreement with experimentally determined liquid-crystal phase relations except where intermediate members of solid solution series, such as melilite and fassaite, are predicted to be in equilibrium with liquid, in which cases liquid-crystal equilibration temperatures are overestimated by 50 to 100 K. CMAS liquids are stable in a solar gas at a P^{tot} at least as low as 5×10^{-2} atm and perhaps as low as 1×10^{-2} atm, much lower than previous estimates for liquids of pure forsterite composition, due to the colligative effects of CaO and Al_2O_3. CMAS liquids are stable at $P^{tot} = 1 \times 10^{-3}$ atm in systems with dust/gas enrichment factors at least as low as 16 and perhaps as low as 5 relative to solar abundances. Results of these calculations suggest that, upon cooling, a solid melilite + spinel condensate assemblage, comparable to a Type A refractory inclusion, would react with the vapor to produce a liquid much richer in MgO and SiO_2 than the starting material, at either elevated P^{tot} or enhanced dust/gas ratio. If this partial melt were isolated from further reaction with the nebular gas, it would solidify into a spinel + melilite + fassaite + anorthite assemblage, similar in chemical and mineralogical composition to a Type B refractory inclusion. Forsterite coexists stably with CMAS condensate liquids over wide ranges of P^{tot} and dust/gas ratio, extending to the lowest P^{tot} and dust/gas ratio at which liquids are stable. If the compositions of glass inclusions inside isolated forsterite crystals in the Murchison CM2 chondrite have been modified by precipitation of 25 wt% forsterite as a daughter mineral from the liquid precursors of those glasses, the inclusions could represent condensate liquids that were in equilibrium with forsterite at $P^{tot} = 0.3$ atm or at dust/gas enrichment factors of ~70 at $P^{tot} = 1 \times 10^{-3}$ atm.

1. INTRODUCTION

The idea that ferromagnesian chondrules are condensates from a solar gas was abandoned when Wood (1963) showed that forsterite could not be in equilibrium with a melt of its own composition in a solar gas unless the total pressure, P^{tot}, were >100 atm, far higher than pressures predicted in hydrodynamic models of the solar nebula. Grossman (1972) showed that the highest-temperature equilibrium condensate assemblages at low P^{tot} are Ca-, Al-rich silicates and oxides which do not contain forsterite. The idea that liquid condensates of some composition could have formed at equilibrium in a solar gas was resurrected when Grossman and Clark (1973) pointed out that the lowest temperature liquids that exist in systems having compositions like those of Grossman's (1972) high-temperature condensates freeze at temperatures only 60 K above the condensation temperatures of those assemblages at 1×10^{-3} atm. Condensation temperatures increase with P^{tot}, and Grossman and Clark (1973) estimated that condensation of that assemblage would occur at its minimum melting temperature at $P^{tot} \sim 5.6 \times 10^{-3}$ atm, only slightly above the maximum pressures thought to be reasonable for the solar nebula. In order to use condensation codes to compute directly the temperatures of appearance of partial melts that may condense at $P^{tot} > 5.6 \times 10^{-3}$ atm and the variation of their composition with temperature, a model relating the activity of each component to the mole fractions of all components in the liquid is required. Both Wood and McSween (1977) and Wagner and Larimer (1978) were aware of the fact that the minimum P^{tot} for stabilization of forsterite + liquid assemblages in a solar gas might be much lower than estimated by Wood (1963) because forsterite is known to coexist stably with silicate liquids of many compositions to temperatures well below the melting point of pure forsterite, and Wagner and Larimer (1978) attempted to model the condensation of liquids in a solar gas by assuming that the liquid is an ideal solution. Wood (1967) was the first to point out that liquid condensates might become stable at low total pressures in gases made by complete vaporization of regions which had become enriched in interstellar dust relative to gas. Bartholomay and Larimer (1982) and Larimer and Bartholomay (1983), using ideal solution approximations, showed that Ca-, Al-, Ti-rich silicate liquids are stable condensates at $P^{tot} = 1 \times 10^{-3}$ atm in systems enriched in dust compared to gas by factors of 20 to 25 relative to solar

* *Present address:* Department of Science and Engineering, National Science Museum, 3-23-1 Hyakunin-cho, Shinjuku-ku, Tokyo 169, Japan.

abundances. Similarly, ideal liquid solution models were used by Wood and Hashimoto (1993) to show that condensate liquids of unspecified composition are in equilibrium with olivine at 1×10^{-5} bar in systems whose dust/gas ratios are enriched by factors of 10^3 to 10^7 relative to solar abundances. Rein and Chipman (1965) and Chamberlin et al. (1992, 1994) have demonstrated experimentally, however, that $CaO-MgO-Al_2O_3-SiO_2$ (CMAS) liquids are highly non-ideal. This means that use of the ideal mixing approximation for liquids in condensation calculations leads to incorrect condensation temperatures, incorrect liquid compositions at each temperature, and liquid-crystal phase assemblages which are in disagreement with known liquid-crystal phase diagrams. Berman (1983) derived an activity-composition model for CMAS liquids which predicts activities of liquid components and liquidus phase relations which are in very good agreement with experimental data. In this paper, we incorporate the Berman (1983) liquid model into condensation calculations, and explore the vapor-solid-liquid stability relations in a solar gas as a function of total pressure, and in cosmic gases as a function of dust/gas ratio at a fixed total pressure of 1×10^{-3} atm. Preliminary versions of this work were presented by Yoneda and Grossman (1994a,b).

2. TECHNIQUE

2.1. Method of Calculation

Equilibrium condensation calculations were performed by solving systems of simultaneous, non-linear, mass-balance equations for sixteen elements (Al, C, Ca, Fe, Mg, N, Na, S, Si, Ti, O, H, Ni, Cr, Co, and He) and mass-action law equations for condensed phases by means of a Newton-Raphson convergence technique as described by Lattimer et al. (1978). Solar abundances of the elements were taken from Anders and Grevesse (1989). The technique is mathematically identical to applying the second-order free energy minimization method to the nonstoichiometric formulation of the equilibrium condition, and can be considered a variation of the BNR algorithm (Smith and Missen, 1982) although our program has the additional capability of treating non-ideal solutions. The computer program, written in FORTRAN 77, is an extensively modified version of the one used by Lattimer et al. (1978). Each calculation was performed at a fixed total pressure and bulk composition, started at a temperature high enough that no condensed phase existed and ended at 900 K. Satisfactory convergence, defined to occur when the left-hand side of each equation is within 10^{-12} of the constant on the right-hand side, is normally obtained within ten iterations. In order to reduce the number of iterations at each temperature, the program uses the phase assemblage of the previous temperature step as a first approximation to the solutions at the current temperature step. Solutions were obtained every ten degrees except when special events occurred, i.e., when a new phase condensed or an existing one disappeared. In such cases, solutions were also obtained at temperatures immediately above and below the event which differ by ≤ 0.1 K. When multiple events occur within a 10 K temperature interval, the program automatically sorts out which event occurs at the highest temperature by successively halving the temperature step until solutions are found which isolate one event from the others under consideration, sometimes leading to temperature intervals < 0.02 K apart. The entire equilibrium description of the system can be computed over a 1000 K temperature interval without operator intervention in $\sim$30 min without non-ideal solutions and in $\sim$2 h with non-ideal solutions using the MS-Windows operating system on an IBM-PC compatible microcomputer with a 66 MHz, 486 chip.

2.2. Treatment of Non-Ideal Solutions

For each of the four non-ideal solutions considered in this study, CMAS liquid, metal alloy, plagioclase, and spinel, the activity coefficient of each component is a non-linear function of mole fraction. Because of this, a special routine had to be used to test for the stability of each of these phases at every temperature step. The difference between the free energy of the solution (a function of composition and activity coefficients) and the free energy of its monatomic gaseous constituents (a function of the mole fractions of the components in the solution and their partial pressures in the gas) was minimized by the quasi-Newton method (Press et al., 1992) by iterating over the mole fractions. For each solution series, this was done from several starting compositions at each temperature step: one at each endmember, one corresponding to an equimolar mixture of all components, and one corresponding to the composition of a hypothetical ideal solution of the same components. A solution phase was considered stable if at least one of the starting compositions converged to a solution phase whose free energy was less than that of its gaseous constituents. Convergence to the same stable composition was normally obtained from multiple starting compositions. After the condensation temperature and initial composition of each non-ideal solution were found, an attempt was made to solve the equation set with the solution phase present at the temperature step immediately above the calculated condensation temperature, using the previously calculated initial composition of the solution phase as a starting approximation to its composition at the higher temperature. This acted as a test of whether the calculated condensation temperature of each non-ideal solution was indeed the highest temperature of its stability, a test which succeeded in every case.

2.3. Thermodynamic Data

All gaseous and condensed species considered and the sources of their thermodynamic data are listed in Table 1. We took all Gibbs free energy of formation data for gaseous species from the JANAF Thermochemical Tables (1985). Most of those for oxide and silicate phases were taken from Robie et al. (1978) unless data for the same phase were given by Robinson et al. (1982), a source which we preferred. Data for additional crystalline phases were taken from more recent experimental determinations and compilations. Where such thermodynamic data are dependent upon data for other species whose values differ from those in the rest of our database, the data were adjusted for compatibility. Results obtained at relatively high pressures, such as 100 atm, should be interpreted with caution, as we have assumed gas ideality and have ignored the pressure dependence of the free energies of condensed phases.

2.4. Data and Modeling for Solid and Liquid Solutions

We assumed that melilite is an ideal, binary, molecular solid solution of gehlenite, Ge, ($Ca_2Al_2SiO_7$) and åkermanite, Åk, ($Ca_2MgSi_2O_7$), as suggested by the data of Charlu et al. (1981). We made the same assumption for solid solution between enstatite ($MgSiO_3$) and ferrosilite ($FeSiO_3$), as suggested by the high-temperature data for Fe-poor orthopyroxenes of Sack (1980). Thermodynamic data for protoenstatite, orthoenstatite, and clinoenstatite were used for the Mg endmember in the temperature interval for the stability of each. Olivine was assumed to be an ideal, ionic solid solution of forsterite (Mg_2SiO_4) and fayalite (Fe_2SiO_4).

Fassaite is modeled as an ideal, molecular solid solution of four components: $CaMgSi_2O_6$ (diopside, Di), $CaAl_2SiO_6$ (Ca-Tschermak's molecule, CaTs), $CaTi^{4+}Al_2O_6$ (Ti-Tschermak's molecule, T_4P), and $CaTi^{3+}AlSiO_6$ (Ti^{3+}-clinopyroxene, T_3P). Free energy data for CaTs were taken from Robinson et al. (1982) and for Di from Robie et al. (1978) as updated by Charlu et al. (1978). For T_4P, the free energy vs. temperature was based on a single thermochemical measurement of ΔG°_f at 1460 K and a molar volume estimate by Beckett (1986), and estimates of the absolute entropy at 298 K and the heat capacity expression by the methods of Holland (1989) and Berman and Brown (1985), respectively. The same technique was employed for T_3P, using a molar volume estimate and the average of three independent thermochemical determinations of $[\Delta G^\circ_f(T_3P) - \Delta G^\circ_f(T_4P)]$ at 1500 K by Beckett (1986), except that the absolute entropy of Ti_2O_3 at 298 K had to be obtained from the heat capacity data of Barin (1989). According to these data, T_4P is $\sim$10 kJ/mol more stable than its constituents, corundum (Al_2O_3)

Table 1. Gaseous and condensed species considered and the sources of their thermodynamic data

Gases [1]

H	O	C	N	Mg	Si	Fe	S	Al	Ca	Na	Ni	Cr
Ti	Co	He	AlN	AlC	AlO	AlO_2	AlS	Al_2O	Al_2O_2	CN	NaCN	CNO
CN_2	CO	COS	CO_2	CS	CS_2	SiC	Si_2C	C_2	C_2N	C_2N_2	$(NaCN)_2$	C_2O
SiC_2	C_3	C_3O_2	C_4	C_4N_2	C_5	CaO	Ca_2	FeO	MgN	MgO	MgS	Mg_2
NO	NO_2	NO_3	NS	SiN	Si_2N	N_2	N_2O	N_2O_3	N_2O_4	N_2O_5	N_3	NaO
Na_2	SO	S_2O	SiO	TiO	O_2	SO_2	SiO_2	TiO_2	O_3	SO_3	SiS	S_2
S_8	Si_2	Si_3	AlOH	AlO_2H	AlH	HCN	HOCN	COH	H_2CO	CH	CH_2	CH_3
CH_4	C_2H_4O	C_2H	C_2H_2	C_2H_4	$Si(CH_3)_4$	CaOH	H_2	$Ca(OH)_2$	$Fe(OH)_2$	MgOH	$Mg(OH)_2$	MgH
HNO	HNO_2	HNO_3	NH	NH_2	NH_3	N_2H_2	N_2H_4	NaOH	NaH	$(NaOH)_2$	OH	H_2O
HO_2	H_2O_2	H_2SO_4	HS	H_2S	SiH	SiH_4						

Pure Solids and Liquids

Al [1]	C (Graphite) [2]	Al_2O_3 (Alpha)[2]*	Mg [1]	Ti [1]	Ca [1]
CaO [2]*	FeO [3]	$Fe_{0.947}O$ [2]	Fe_2O_3 [2]	Fe_3O_4 [2]	MgO [2]*
NaO_2 [1]	Na_2O [1]	Na_2O_2 [1]	SiO_2 (Beta Quartz) [2]*	SiO_2 (Cristobalite) [2]*	$CaTiSiO_5$ [3]
TiO (Beta) [1]	TiO_2 (Rutile) [3]	Ti_2O_3 [3]	Ti_3O_5 [3]	Ti_4O_7 [3]	$MgFe_2O_4$ [3]
$CaAl_{12}O_{19}$ [4]*	$CaAl_4O_7$ [4]*	$CaAl_2O_4$ [5]*	$Ca_{12}Al_{14}O_{33}$ [5]	$Ca_3Al_2O_6$ [5]*	$CaTiO_3$ [3]
$FeTiO_3$ [3]	$MgTiO_3$ [3]	$MgTi_2O_5$ [1]	Mg_2TiO_4 [1]	$NaAlO_2$ [1]	CaS [1]
FeS [3]	FeS_2 [1]	MgS [1]	Na_2S [1]	SiS_2 [1]	NaH [1]
MgH_2 [1]	TiH_2 [1]	Al_4C_3 [1]	Fe_3C [3]	MgC_2 [1]	Mg_2C_3 [1]
SiC (Beta) [1]	TiC [1]	Mg_2Si [1]	AlN [1]	Mg_3N_2 [1]	Si_3N_4 [1]
TiN [1]	$CaSO_4$ [3]	NaCN (liquid) [1]	$CaCO_3$ [2]	$MgCO_3$ [2]	Si_2N_2O [6]
Na_2CO_3 (liquid) [1]	$FeSO_4$ [1]	$Fe_2(SO_4)_3$ [1]	$MgSO_4$ [1]	Na_2SO_4 [3]	$NaAlSiO_4$ [3]
$CaSiO_3$ (Pseudowollastonite) [7]*	$CaSiO_3$ (Wollastonite) [7]*	$Ca_3Al_2Si_3O_{12}$ [2]*	Ca_3SiO_5 [2]*	$Ca_3MgSi_2O_8$ [3]*	$Na_2Si_2O_5$ [1]
Ca_2SiO_4 (Larnite) [2]*	Ca_2SiO_4 (Alpha) [2]*	Ca_2SiO_4 (Alpha') [2]*	Ca_2SiO_4 (Ca-Olivine) [2]	$Ca_3Si_2O_7$ [2]*	Na_2SiO_3 [1]
$NaAlSi_2O_6$ [3]	$Mg_3Al_2Si_3O_{12}$ [3]	$Mg_2Al_4Si_5O_{18}$ [3]	$Mg_7Si_8O_{22}(OH)_2$ [2]	$Mg_3Si_4O_{10}(OH)_2$ [2]	$Al_6Si_2O_{13}$ [3]
Al_2SiO_5 (Sillimanite) [2]*	Al_2SiO_5 (Kyanite) [2]*	Al_2SiO_5 (Andalusite) [2]*	SiO_2 (Alpha Quartz) [8]	SiO_2 (Tridymite) [8]	$CaMgSiO_4$ [8]
$Mg_4Al_{10}Si_2O_{23}$ [8]	Cr_2O_3 [1]				

Solutions

CMAS Liquid [8]:	$CaO_{(l)}$ - $MgO_{(l)}$ - $Al_2O_{3(l)}$ - $SiO_{2(l)}$	Metal [1]:	Si - Cr - Co - Ni - Fe (Gamma)
Melilite:	$Ca_2MgSi_2O_7$ [9]* - $Ca_2Al_2SiO_7$ [2]*	Olivine:	Fe_2SiO_4 [2] - Mg_2SiO_4 [2]*
Ca-poor Pyroxene:	$FeSiO_3$ [2] - $MgSiO_3$ [2]*	Plagioclase:	$NaAlSi_3O_8$ [3] - $CaAl_2Si_2O_8$ [2]*
Fassaite:	$CaAl_2SiO_6$ [2] - $CaTiAlSiO_6$ [10] - $CaTiAl_2O_6$ [10] - $CaMgSi_2O_6$ [11]*		
Spinel:	$FeAl_2O_4$ [12] - $MgCr_2O_4$ [12] - $MgAl_2O_4$ [13]* - $FeCr_2O_4$ [12]		

Sources:
[1] JANAF Thermochemical Tables (1985)
[2] Robinson et al. (1982)
[3] Robie et al. (1978)
[4] Geiger et al. (1988)
[5] Allibert et al. (1981)
[6] Fegley (1981)
[7] Richet et al. (1991); Zhu et al. (1994)
[8] Berman (1983)
[9] Charlu et al. (1981)
[10] Beckett (1986); Holland (1989); Berman and Brown (1985); also see text
[11] Charlu et al. (1978)
[12] Sack and Ghiorso (1991)
[13] Chamberlin et al. (1995a)

* Data from Berman (1983) are used when CMAS liquid is stable

+ perovskite ($CaTiO_3$), so stable, for example, that pure T_4P condenses at 1700 K at $P^{tot} = 1 \times 10^{-3}$ atm. Pure T_4P is unknown. Yagi and Onuma (1967) found a maximum X_{T_4P} of 0.10 in pyroxenes synthesized along the Di-T_4P join, and Onuma and Kimura (1978) found $X_{T_4P} = 0.24$ with $X_{CaTs} = 0.08$ in the Di-CaTs-T_4P ternary, suggesting that solid solution of CaTs enhances the solubility of T_4P. Yang (1976) reported X_{T_4P} as high as 0.31 in the same system. Allende fassaite is also known with X_{T_4P} up to 0.20 when $X_{CaTs} = 0.05$ and $X_{T_4P} = 0.27$ (Beckett, 1986). Assuming that the latter formed at equilibrium, 20 mol% may be the maximum solubility of T_4P in such quaternary pyroxenes. We thus increased $\Delta G^{\circ}_f(T_4P)$ at 1500 K by 13.9 kJ/mol, reducing its stability by just enough that no pyroxene composition calculated herein had $X_{T_4P} > 0.20$. Although this is somewhat arbitrary, the relative stability of T_4P and T_3P, and therefore the calculated Ti^{3+}/Ti^{4+} ratio in fassaite, is not affected.

Free energy data for spinel, sp ($MgAl_2O_4$) were taken from Chamberlin et al. (1994) and, for each of hercynite, hc ($FeAl_2O_4$), picrochromite, pc ($MgCr_2O_4$), and chromite, ch ($FeCr_2O_4$), were calculated from the enthalpy and entropy of formation from the elements at 298 K and the heat capacity vs. temperature function of Sack and Ghiorso (1991). Because spinel is a reciprocal solid solution, its composition can be calculated using the free energies of any three of the above four components in an ideal solution model, as was done by Simon et al. (1994) and Yoneda and Grossman (1994a,b). In reality, however, the free energy of a spinel of intermediate composition is a function of the free energies of the four components which are independent of one another. A convenient way of constraining the spinel composition by all four free energies was derived by Wood and Nicholls (1978) and is adopted here. In it, the fourth free energy is used to calculate a contribution to the activity coefficient for each of the endmember components. As in Webb and Wood (1986), the only significant non-ideal solution effect is assumed to be due to Cr-Al mixing, and the Margules parameter for this effect measured by Webb and Wood (1986) is used in a regular solution model herein to calculate the remaining contribution to each activity coefficient. The activity-composition relations are $a_{sp} = X_{Mg}X^2_{Al}\gamma_{sp}$, $a_{hc} = X_{Fe}X^2_{Al}\gamma_{hc}$, $a_{pc} = X_{Mg}X^2_{Cr}\gamma_{pc}$, and $a_{ch} = X_{Fe}X^2_{Cr}\gamma_{ch}$, where a_i and γ_i are the activity and activity coefficient, respectively, of component i, X_{Mg} and X_{Fe} are the atom fractions in the tetrahedral site, and X_{Al} and X_{Cr} are the atom fractions in the octahedral site.

We also explored the non-ideal, ionic, binary solid solution between Al_2O_3 and $MgAl_2O_4$ as a function of P^{tot} at 1673 K. Because reliable activity data for this solid solution exist only at that temperature, we did not include it in the calculations presented herein. The coexisting phase assemblage is unaffected when this solid solution is incorporated into condensation calculations at 1673 K, and the results are reported by Chamberlin et al. (1995b).

Plagioclase was treated as a non-ideal, binary solid solution between anorthite, An ($CaAl_2Si_2O_8$) and albite, Ab ($NaAlSi_3O_8$), using the Al-avoidance model and excess enthalpy of mixing data for high plagioclase from Newton et al. (1980). A five-component solid metal alloy of Fe, Ni, Co, Cr, and Si was treated non-ideally using the same data as in Grossman et al. (1979). At the very highest total pressures encountered in this work, use of these thermodynamic data leads to condensation of metal alloys of very high Ni content at very high temperatures. Although the presence of significant amounts of Si, Co, and Cr in the computed alloys complicates the liquid-crystal phase relations, it is likely that the highest-temperature, highest-Ni solid alloys predicted to condense at $P^{tot} \geq 0.3$ atm form, in reality, under conditions where they would be at least partially molten, a complication which we have neglected.

Berman (1983) derived an activity-composition model, the Margules parameters for which also appear in De Capitani and Brown (1987), applicable to the entire composition range of CMAS liquids. This system is known to be very important in high-temperature condensation processes, a factor which distinguishes the Berman (1983) model from other solution models for silicate liquids such as those of Ghiorso et al. (1983) and Blander and Pelton (1987) that are restricted to geologically relevant compositions and Al_2O_3-free systems, respectively. The Berman (1983) model is based upon

Table 2. Comparison of Temperatures From Different Condensation Calculations

	This work			Lattimer et al. (1978)			Wood & Hashimoto (1993)	
	in (K)	*out (K)*		*in (K)*	*out (K)*		*in (K)**	*out (K)**
Corundum	1770	1740		1742	1530		1763	1753
Hibonite	1743	1500					1753	1532
Corundum							1532	1516
Perovskite	1688	1448		1680	1405			
Melilite ss**	1628	1444		1625	1435		1655	1417
Al-Spinel ss	1501	1409	pure sp	1535	1385	sp-hc	1516	1398
Metal ss	1464		pure Fe	1450		Fe-Si	1460	
Fassaite ss	1449		pure Di	1435		Di-CaTs	1417	
Forsterite	1443			1430			1460	
Plagioclase ss	1416		pure An	1385	1068		1400	
Ti_3O_5	1386	1361		1405	1265			
Enstatite	1366			1350			1378	
Ti_4O_7	1361	1217		1265	1105			
Cr-Spinel ss	1221							
Sphene	1217			760				
TiO_2				1105	760			
Abundances	Anders & Grevesse (1989)			Cameron (1973)			Anders & Grevesse (1989)	
P^{tot}	10^{-3} atm with He			10^{-3} atm with He			10^{-3} bar without He	

* ±5 K uncertainty in reading from Fig. 2 of Wood and Hashimoto (1993).
** In this table, ss is used to indicate solid solution phases which depart significantly from end-member compositions in the temperature range of interest.

thermodynamic data for pure solids and solid-solid reactions, and from the temperatures and compositions of liquids known to be in equilibrium with various individual solid phases and phase assemblages. Omission of Ti from the Berman (1983) model, however, means that our incorporation of this model into condensation calculations artificially forces Ti to condense into solid phases under conditions where one might expect it to dissolve in the coexisting liquid. The main advantages of the Berman (1983) model are that it reproduces the liquidus phase relations very well and predicts activities of liquid components which are in very good agreement with experimental measurements (Rein and Chipman, 1965; Chamberlin et al., 1992, 1994) in the near-liquidus temperature regime within which the equilibria upon which the model is based are pinned. Because these agreements break down when the Berman (1983) model is extrapolated to temperatures far above the liquidus (Barron, 1985, 1986), we urge caution in interpreting the results presented herein for the highest-temperature liquids at P^{tot} = 100 and 10 atm and at dust/gas ratio enhancements of 10^3 at $P^{tot} = 1 \times 10^{-3}$ atm, where the initial liquids form at ~400, ~300, and ~200 K above the liquidus, respectively. All liquids predicted in this work at $P^{tot} \leq 1.5$ atm and at dust/gas ratio enhancements $\leq$ 300 at $P^{tot} = 1 \times 10^{-3}$ atm form within 100 K of the liquidus where the Berman (1983) model works well. An exception to this general rule occurs when intermediate members of solid solution series, such as melilite, are predicted to be in equilibrium with condensate liquids. Because thermodynamic data for the liquid in Berman's (1983) model are based only on thermodynamic data for pure endmembers and never on those for intermediate members of solid solution series, agreement between calculated solid solution-liquid equilibration temperatures and experimentally determined temperatures for the same equilibria is much poorer than for equilibria involving liquids and pure endmember solids.

The Berman (1983) liquid model is based necessarily on pre-1984 literature sources for thermodynamic data for solid phases. Despite our preference for the sources given in Table 1 for thermodynamic data for solids, for consistency purposes, we had to substitute thermodynamic data for twenty-nine solid phases used in the Berman (1983) model for data for the same phases given in Table 1 whenever the latter model was used in our condensation calculations. Use of the modified dataset at $P^{tot} = 1 \times 10^{-3}$ atm, where there are no stable liquids, results in partial replacement of the hibonite ($CaAl_{12}O_{19}$) field by $CaAl_2O_4$ and $CaAl_4O_7$, which delays the appearance of melilite by 35 K, but the condensation temperatures of all other species are within ±6 K of those calculated using the original data. Using the replaced dataset, we found that CMAS liquids are stable in a solar gas at $P^{tot} \geq 5 \times 10^{-2}$ atm and at dust/gas enrichment factors $\geq$ 16 relative to the solar abundances at $P^{tot} = 1 \times 10^{-3}$ atm. Under all other conditions, the original thermodynamic dataset was used.

2.5. Compositions of Dust-Enriched Systems

The compositions of dust-enriched systems were calculated under the assumption that none of the H, He, C, and N but all of the Al, Ca, Mg, Na, Si, Ti, Cr, Co, and Ni were in the dust. All S was assumed to have condensed into the dust as FeS as well as all of the remaining Fe as FeO. The fraction of the oxygen in the dust was calculated stoichiometrically. This is equivalent to considering the dust to have the bulk composition of the material which condenses at equilibrium from a gas of solar composition at ~500 K at $P^{tot} = 1 \times 10^{-3}$ atm. Even if conditions were such that some of the iron was metallic, the overestimate of the abundance of oxygen in dust-enriched systems resulting from the above assumption is small, as the total amount of oxygen allocated to FeO is $\leq$10% of the total oxygen in all dust-enriched systems studied here.

3. CONDENSATES AT 10^{-3} ATM TOTAL PRESSURE

3.1. Condensation Sequence

The calculated temperatures of condensation and disappearance of major element-containing phases at a total pressure of 1×10^{-3} atm are given in the first and second columns of Table 2, respectively, and the corresponding distributions of Al, Ca, Mg, and Si between crystalline phases and vapor are illustrated in Fig. 1a,b,c, and d, respectively. Corundum condenses at 1770 K and begins to react with the gas to form hibonite at 1743 K, disappearing completely at 1740 K. Perovskite condenses at 1688 K and accounts for 90% of the Ti by 1645 K. Almost all of the Al is present as hibonite when the latter begins to react with the gas to form gehlenite at 1628 K. The gehlenite/hibonite ratio increases progressively with falling temperature until 1525 K, where 99% of the Ca is condensed. At 1500 K, the remaining hibonite reacts completely with gaseous Mg to form nearly pure $MgAl_2O_4$ and a small amount of gehlenite. Below this temperature, gehlenitic melilite reacts with gaseous Mg to form more åkermanite-rich melilite and spinel. The åkermanite content of melilite rises from 1 mol% at 1495 K to 39 mol% at 1450 K, causing the proportion of the total aluminum accounted for by melilite to fall from 68 to 42%. A metal alloy consisting of Fe, Ni, Co, Cr, and Si condenses at 1464 K. Melilite, perovskite, and a small amount of spinel begin to react with gaseous Mg and

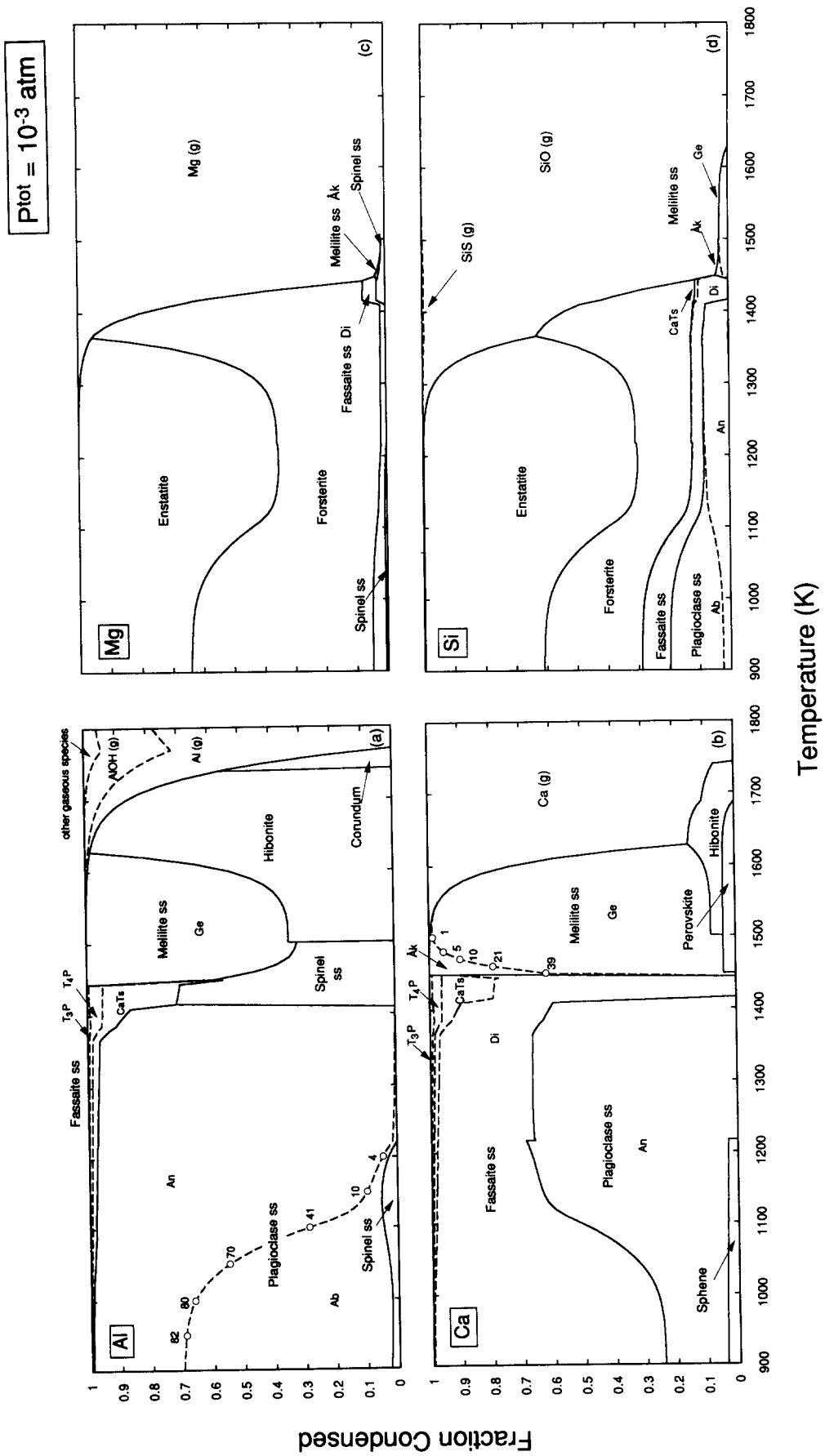

FIG. 1. The distribution of (a) Al, (b) Ca, (c) Mg, and (d) Si between condensed phases and vapor as a function of temperature in a gas of solar composition at $P^{tot} = 1 \times 10^{-3}$ atm. Dashed curves separate the gas phase into different species and solid solution fields into endmember components. Solid solution phases containing significant amounts of more than one endmember under the conditions portrayed are indicated by the abbreviation ss. Numbers on curve separating An field from Ab field in (a) represent mol% Ab in plagioclase ss. Those on curve separating Ge from Åk in (b) represent mol% Åk in melilite ss. Abbreviations: ss, solid solution; g, gas; Ge, gehlenite; Åk, åkermanite; Di, diopside; CaTs, Ca-Tschermak's molecule; T_3P, Ti^{3+}-bearing pyroxene; T_4P, Ti^{4+}-bearing pyroxene; An, anorthite; Ab, albite.

Si to form fassaite, a Ca-rich clinopyroxene containing Al, Ti^{3+}, and Ti^{4+}, at 1449 K, consuming perovskite at 1448 K and melilite ($Åk_{49}$) at 1444 K. Forsterite condenses at 1443 K and accounts for 94% of the Mg and 50% of the Si when it begins to react with the remaining gaseous Si to form protoenstatite at 1366 K. Meanwhile, spinel and fassaite begin reacting with one another to form anorthite at 1416 K, causing spinel to disappear at 1409 K. The enstatite/forsterite ratio gradually increases with falling temperature until 1180 K. At 1386 K, Ti is expelled from fassaite as Ti_3O_5 which, in turn, is oxidized to Ti_4O_7 at 1361 K. At 1221 K, Cr in the metal alloy begins to react with plagioclase and magnesium silicates to form a spinel solid solution which is much richer in $MgCr_2O_4$ than the spinel phase that forms at higher temperature. Such Cr-rich spinel solid solutions were not predicted in previous condensation calculations. This is mainly due to the fact that the stability of $MgCr_2O_4$-bearing spinel was not previously investigated in a solar gas in this temperature range, although Krot et al. (1993) attempted to estimate its stability without doing a full equilibrium calculation. Finally, Ti_4O_7 reacts completely with a small amount of fassaite to form sphene at 1217 K. For the variation with temperature of the compositions of phases which are solid solutions, see the curves for $P^{tot} = 1 \times 10^{-3}$ atm in Figs. 7–11.

3.2. Comparisons with Previous Work

In Table 2, the temperatures of condensation and disappearance calculated in this work at 1×10^{-3} atm total pressure are compared with those in previous computations at this total pressure by Lattimer et al. (1978) and Wood and Hashimoto (1993). Had the same thermodynamic data been used in all three efforts, the condensation temperatures of oxygen-containing phases calculated herein would all be expected to be higher by ~18 K than in the work of Lattimer et al. (1978) due to the higher atomic O/H ratio, 8.53×10^{-4}, in the solar system abundance table of Anders and Grevesse (1989), which is used in the present work, than in the Cameron (1973) table, 6.76×10^{-4}, used in Lattimer et al. (1978). Similarly, even though the Anders and Grevesse (1989) abundances were used in both Wood and Hashimoto (1993) and this work, all condensation temperatures calculated herein would still be expected to be lower than those in Wood and Hashimoto (1993) by ~7 K, due to the fact that we have included the diluting effect of He on the partial pressures of the condensable elements, an element omitted from the calculations of Wood and Hashimoto (1993). Because inspection of Table 2 does not reveal such systematic differences, we re-ran our program twice, once using the thermodynamic data employed by Lattimer et al. (1978) and once with the data used by Wood and Hashimoto (1993), in order to make sure that the discrepancies seen in Table 2 are due solely to differences in thermodynamic data rather than to more fundamental problems such as the resolving power of the programs or convergence difficulties. Satisfactory agreement was obtained in all cases except that our calculation, using the same thermodynamic and abundance data as are given by Wood and Hashimoto (1993), yields a condensation temperature for plagioclase which is 45 K higher than the result given in that paper. With this exception in mind, the reader can estimate the sensitivity of condensation temperatures to variations in thermodynamic data by comparing condensation temperatures in the present work with those of Wood and Hashimoto (1993) after subtracting ~7 K from the latter, or by comparing those in the present work with those of Lattimer et al. (1978) after adding ~18 K to the latter.

4. VARIATION OF CONDENSATION SEQUENCE WITH TOTAL PRESSURE

4.1. Overview

Except for the molecular species of elements which are at least partly condensed, the partial pressures of most species at a given temperature are proportional to the total pressure of the gas. Thus, at a low total pressure, the partial pressures of the molecular species containing condensable elements are further below their saturation values at each temperature than at some higher total pressure. This causes the condensation temperature of an element to increase or decrease with the total pressure of the gas. If the total pressure is high enough, the calculated condensation temperatures of solid condensates exceed their melting points, and condensation of partial melts will occur instead. We have found that condensation of partial melts does not occur in a gas of solar composition until total pressures at or above 5×10^{-2} atm are reached. Since the thermodynamic data for solid phases that must be used when the Berman (1983) liquid model is employed in our computations differ from those used when only solids condense, and since the entire character of the condensates changes when liquids condense, we divide this discussion into two pressure regimes, $P^{tot} < 5 \times 10^{-2}$ atm and $P^{tot} \geq 5 \times 10^{-2}$ atm.

4.2. Condensation at Total Pressures $< 5 \times 10^{-2}$ atm

The calculations were carried out at total pressures of 1×10^{-2}, 1×10^{-4}, 1×10^{-5}, and 1×10^{-6} atm using exactly the same input data and computer program as at 1×10^{-3} atm. Results are summarized in Table 3 and Fig. 2, where it is seen that, with few exceptions, condensation temperatures all increase with increasing P^{tot} and condensation curves are nearly parallel to one another. The result is that the condensation sequence is nearly the same over the entire pressure range investigated. Only the exceptions to this general rule are discussed here.

The range of temperature of corundum stability gradually narrows with increasing P^{tot} such that, at 1×10^{-2} atm, it has no stability field. Instead, hibonite is the first condensate. It forms at 1846 K and begins to react with gaseous Ca to form $CaAl_2O_4$ at 1724 K. The latter phase is completely consumed by melilite at 1711 K. The temperature interval between fassaite and forsterite condensation also narrows with increasing P^{tot}, such that forsterite actually condenses at a higher temperature than fassaite, 1525 vs. 1524 K, at this pressure.

As seen in previous work (Grossman, 1972), the condensation curves for metallic nickel-iron and forsterite cross, with metal condensing at a higher temperature than forsterite at $P^{tot} > 1 \times 10^{-4}$ atm.

At total pressures below 1×10^{-3} atm, a number of reactions among Ca- and Al-rich phases occur which are distinct from those at 1×10^{-3} atm. Only some of these are illustrated

Table 3. Temperatures of appearance and disappearance of stable condensates at several representative total pressures in the pressure regime where liquids are not stable.

Condensate \ P^{tot} (atm)	1×10^{-6}		1×10^{-5}		1×10^{-4}		1×10^{-3}		1×10^{-2}	
	In	Out	In	Out	In	Out	In	Out	In	Out
Corundum	1571	1481	1633	1558	1699	1643	1770	1740		
Hibonite	1485	1292	1562	1350	1647	1421	1743	1500	1846	1590
Perovskite	1471	1257	1537	1317	1609	1380	1688	1448	1775	1523
$CaAl_2O_4$									1724	1711
Melilite ss	1405	1264	1472	1318	1546	1377	1628	1444	1711	1505
Corundum	1292	1286								
Spinel ss	1286	1266	1351	1315	1421	1343	1501	1409	1591	1481
Plagioclase ss	1268	1250	1320	1310						
Rankinite	1264	1255	1318	1313	1377	1375				
Fassaite ss	1257		1317		1380		1449		1524	
Spinel ss	1252	1227	1313	1283						
Forsterite	1246		1305		1371		1443		1525	
Plagioclase ss	1234		1289		1350		1416		1488	
Sphene			1270	1252						
Enstatite	1195		1246		1303		1366		1435	
Spinel ss	1161		1196		1217		1221		1219	
Ti_3O_5							1386	1361	1454	1358
Ti_4O_7			1252	1217	1324	1216	1361	1217	1358	1220
Sphene	1222		1217		1216		1217		1220	
Metal	1214		1287		1370		1464		1574	

in Fig. 2. Complete results are shown in Table 3. The reaction of hibonite with gaseous Mg to form nearly pure $MgAl_2O_4$ and melilite is replaced by a reaction between hibonite and $SiO_{(g)}$ to form corundum and gehlenite at 1292 K at 1×10^{-6} atm total pressure, yielding a second corundum stability field at a lower temperature than the usual one. The corundum so formed, however, reacts completely with gaseous Mg to form spinel at 1286 K, making this stability field only 6 K wide at this pressure. It pinches out completely at a pressure below 1.0×10^{-5} atm. Below 2.0×10^{-5} atm, spinel and melilite react to form anorthite at a higher temperature than that for fassaite formation, yielding a second anorthite field at a higher temperature than the usual one. At a slightly lower temperature but still above the temperature of first appearance of fas-

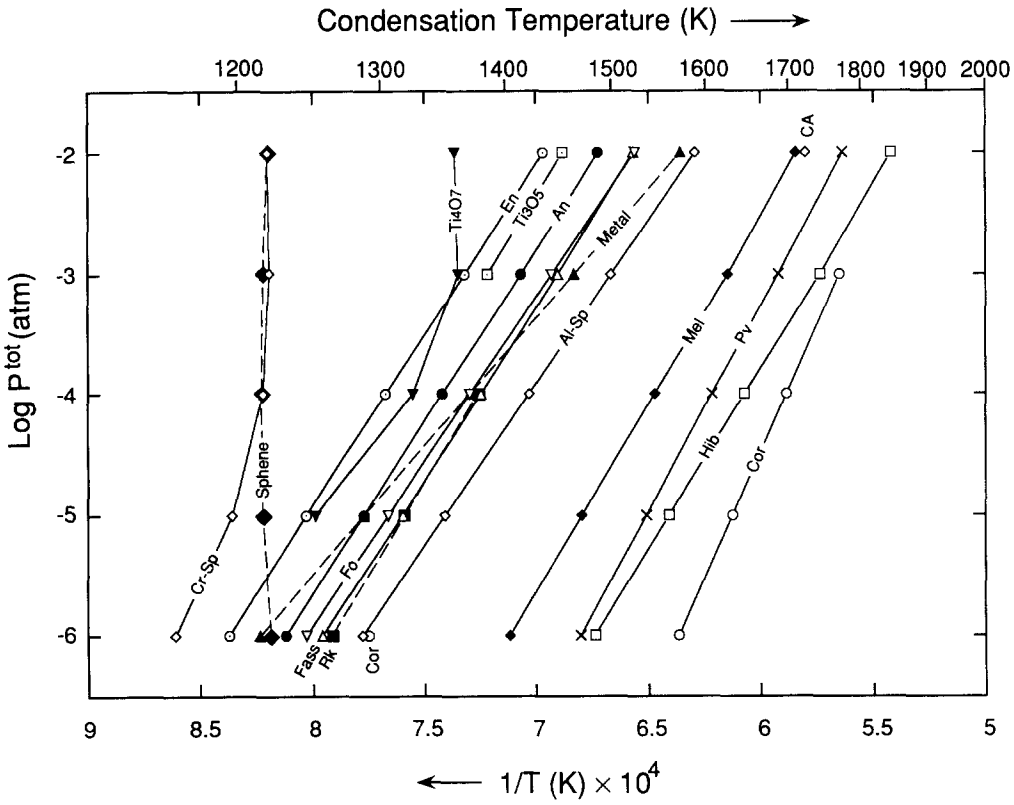

FIG. 2. Variation of condensation temperatures of most high-temperature condensate minerals with total pressure in the range of total pressures where condensate liquids are absent. Cor, corundum; Hib, hibonite; Pv, perovskite; CA, $CaAl_2O_4$; Mel, melilite; Al-Sp, high-temperature, $MgAl_2O_4$-rich spinel; Rk, rankinite; Fass, fassaite; Fo, forsterite; En, enstatite; Cr-Sp, low-temperature, $MgCr_2O_4$-rich spinel. Other abbreviations as used previously.

saite at these pressures, melilite decomposes completely to form rankinite ($Ca_3Si_2O_7$), anorthite, and, above 3.5×10^{-6} atm, spinel. Below 2.0×10^{-5} atm, fassaite then forms by reaction between rankinite, perovskite, anorthite, and, above 3.5×10^{-6} atm, spinel, consuming perovskite first, then spinel, if present, and then rankinite in a narrow temperature interval, from 1317 to 1313 K at 1×10^{-5} atm and from 1257 to 1255 K at 1×10^{-6} atm. The sequence at 1×10^{-4} atm is slightly different from that at 1×10^{-3} atm in that a narrow field of rankinite is present, and also different from the one below 2.4×10^{-5} atm in that rankinite forms below, rather than above, the temperature of first appearance of fassaite, in this case when melilite decomposes completely into rankinite, spinel and fassaite at 1377 K. Rankinite then reacts completely with CaTs to form spinel and diopside at 1375 K.

4.3. Condensation at Total Pressures $\geq 5 \times 10^{-2}$ atm

Calculated temperatures of appearance and disappearance of condensates stable at several discrete total pressures above 5×10^{-2} atm are shown in Table 4.

4.3.1. $P^{tot} = 0.3$ atm

The calculated distributions of Al, Ca, Mg, and Si between condensed phases and vapor in a gas of solar composition at $P^{tot} = 0.3$ atm are shown in Fig. 3a,b,c, and d, respectively. The variation with temperature of the compositions of liquid and solid solutions can be found in Figs. 6, 7, 8, 9, 10, and 11. $CaAl_4O_7$ begins to condense at 1971 K, followed by perovskite at 1915 K. At 1885 K, where $CaAl_4O_7$ accounts for 88% of the Al and only 31% of the Ca, a liquid begins to condense which has the composition 49.9 mol% CaO, 0.3% MgO, 45.5% Al_2O_3, and 4.3% SiO_2. As the temperature falls, CaO, MgO, Al_2O_3, and SiO_2 continue to condense into the liquid and $CaAl_4O_7$ gradually dissolves into it. At 1798 K, $CaAl_4O_7$ has almost completely disappeared and the liquid now accounts for 86% of the Ca, 97% of the Al, and only 1.6% of the Si. At this point, the liquid freezes to a mixture of gehlenitic melilite and $CaAl_4O_7$. As the temperature falls, $CaAl_4O_7$ gradually reacts with gaseous Ca, Mg, Al, and Si to form more melilite. A metal alloy condenses at 1771 K, containing 15.1 mol% Ni, 0.5% Co, 0.3% Cr, and 1.3% Si. At 1735 K, $CaAl_4O_7$ reacts completely with gaseous Mg and Si to form virtually pure $MgAl_2O_4$ and more melilite. With falling temperature, gaseous Mg and Si react with melilite, increasing its Åk content which lowers the minimum melting temperature of the assemblage, and producing more spinel. When X_{Ak} in the melilite reaches 0.38 at 1680 K, melilite and spinel react with gaseous Mg and Si to form a liquid, and melilite dissolves into it completely by 1678 K. At this point, the liquid contains 33.3% CaO, 15.4% MgO, 12.9% Al_2O_3, and 38.4% SiO_2. As the temperature falls, more Mg and Si condense into the liquid. At 1664 K, forsterite begins to condense from the gas, consuming 77% of the Mg by 1600 K. While forsterite condenses, Si continues to condense into the liquid, spinel gradually dissolves into the liquid and the MgO content of the liquid falls. At 1638 K, perovskite reacts to form Ti_2O_3 which, in turn, reacts to form Ti_3O_5 at 1607 K. At 1588 K, the liquid has the composition 20.1 mol% CaO, 22.8% MgO, 11.6% Al_2O_3, and 45.5% SiO_2 just before the spinel is consumed in a reaction with the liquid to form plagioclase. With forsterite condensation continuing to consume gaseous Mg and Si, SiO_2 continues to condense into the liquid between 1587 and 1540 K, while the proportion of the Mg accounted for by the liquid decreases from 4.6% at 1587 to 4.0% at 1570 and then steadily increases, reaching 7.9% at 1540 K. Simultaneously, plagioclase forms at the expense of the liquid until the temperature falls to 1570 K and is then gradually consumed by the liquid, its Ab content reaching 2 mol% just before disappearing completely at 1540 K. At this point, all Ca and Al in the system are in the liquid phase. At 1536 K, forsterite begins to react with the gas to form protoenstatite, causing removal of virtually all of the remaining Mg and Si from the gas by 1400 K. Some protoenstatite also precipitates from the liquid. Meanwhile, at 1532 K, plagioclase begins crystallizing from the liquid and, at 1523 K, the liquid reacts with some of the Ti_3O_5 and disappears completely, replaced by a mixture of more plagioclase and fassaite

Table 4. Temperatures of appearance and disappearance of stable condensates at several representative total pressures in the pressure regime where liquids are stable.

Condensate \ P^{tot} (atm)	0.1		0.3		1		1.5	
	In	Out	In	Out	In	Out	In	Out
$CaAl_4O_7$	1928	1788	1971	1735	2020	1945		
Perovskite	1866	1594	1915	1637	1968	1724	1986	1747
CMAS liquid			1885	1798	1991	1781	2038	1527
$CaAl_2O_4$	1826	1766						
Melilite ss	1776	1620	1798	1678	1821	1758		
$CaAl_4O_7$	1766	1685						
Spinel ss	1685	1558	1735	1587	1781	1631	1797	1652
CMAS liquid	1622	1560	1680	1523	1760	1526		
Forsterite	1617		1664		1717		1736	
Plagioclase ss	1562		1588	1540				
Enstatite	1509		1536		1576		1589	
Plagioclase ss			1532		1535		1537	
Fassaite ss	1594		1523		1526		1527	
Spinel ss	1218		1217		1226		1233	
Ti_2O_3			1638	1607	1724	1603	1747	1602
Ti_3O_5	1531	1358	1607	1358	1603	1360	1602	1363
Ti_4O_7	1358	1155	1358	1160	1360	1180	1363	1188
$MgTi_2O_5$	1155	1148	1160	1152	1180	1155	1188	1156
Sphene	1148		1152		1155		1156	
Metal	1701		1771		1854		1884	

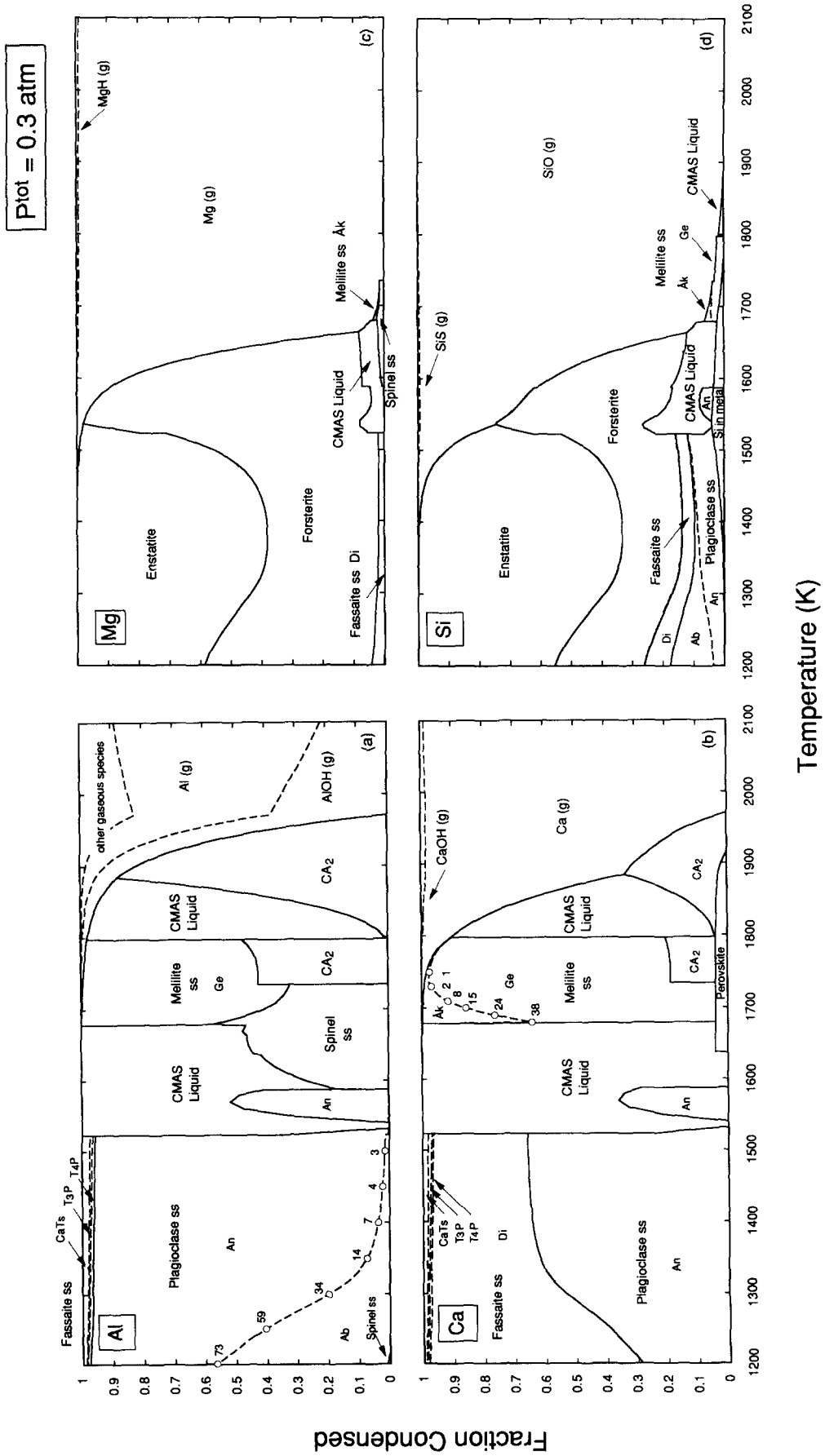

FIG. 3. The distribution of (a) Al, (b) Ca, (c) Mg, and (d) Si between condensed phases and vapor as a function of temperature in a solar gas at P^{tot} = 0.3 atm. Liquids are stable at this total pressure, but condensation temperatures are so close to solidus temperatures that the temperature interval for the stability of liquid is split in two by the intervention of a completely solid assemblage which actually melts upon further cooling. Note the stable coexistence of forsterite and liquid and the small temperature intervals over which all of the Al and Ca are in the liquid. CA_2, $CaAl_4O_7$; CMAS Liquid, a liquid containing CaO, MgO, Al_2O_3, and SiO_2. Conventions and other abbreviations as in Fig. 1.

having $X_{CaTs} = 0.052$, $X_{T_3P} = 0.036$, and $X_{T_4P} = 0.017$. As the temperature falls, the fassaite becomes slightly lower in Al and Ti^{3+} and slightly higher in Ti^{4+}, the plagioclase becomes more sodic and the metal phase becomes richer in Cr and poorer in Si. At 1358 K, Ti_3O_5 is oxidized to Ti_4O_7 with no perceptible effect on the composition of the coexisting fassaite. At 1250 K, X_{Fa} in olivine is 0.002, all Cr is condensed into the metal phase, and plagioclase has reached the composition $X_{Ab} = 0.59$. At 1217 K, Cr in the metal alloy reacts with plagioclase and magnesium silicates to form a spinel solid solution whose X_{Cr} and X_{Fe}, 0.83 and 0.009, respectively, are both much higher than those of the higher-temperature spinel.

4.3.2. $P^{tot} = 1.5$ atm

At total pressures above 0.3 atm, condensation temperatures are raised even higher above the solidus, resulting in broader and more continuous temperature intervals over which liquids are stable. For example, compare the distributions of Al, Ca, Mg, and Si between condensed phases and vapor at 1.5 atm in Fig. 4a,b,c, and d, respectively, with their counterparts in Fig. 3a,b,c, and d, respectively. The liquid field is so extensive at 1.5 atm total pressure that it completely replaces the fields of melilite, corundum, hibonite, and other calcium aluminates which are condensates at lower total pressures. The highest-temperature condensate at $P^{tot} = 1.5$ atm is a liquid which forms at 2038 K and contains 41.2 mol% CaO, 0.2% MgO, 57.6% Al_2O_3, and 1.0% SiO_2. The steepness of the condensation curves in these figures decreases in the order Al, Ca, Si, and Mg, causing the Al_2O_3 content of the liquid to fall continuously with decreasing temperature, the SiO_2 and MgO contents to rise continuously and the CaO content to rise to a maximum of 48.4% at 1920 K and to fall continuously below that temperature. Meanwhile, perovskite condenses at 1986 K and a metal phase, whose initial composition is 14.8 mol% Ni, 0.4% Co, 0.3% Cr, and 2.0% Si, at 1884 K. At 1797 K, Al_2O_3 in the liquid begins to react with gaseous Mg to form nearly pure $MgAl_2O_4$. As the temperature falls, Mg and Si continue to condense into the liquid. Spinel continues to form from the liquid until the temperature falls to 1750 K whereafter spinel gradually dissolves in the liquid with decreasing temperature. Perovskite reacts completely to form Ti_2O_3 at 1747 K. After the liquid reaches 19.2 mol% CaO, 34.5% MgO, 9.6% Al_2O_3, and 36.8% SiO_2 at 1736 K, forsterite becomes stable, both condensing from the gas and crystallizing from the liquid. The last spinel dissolves in the liquid at 1652 K. Ti_2O_3 is oxidized to Ti_3O_5 at 1602 K. The metal phase reaches its maximum Si content at 1589 K, where it contains 4.8 mol% Ni, 0.2% Co, 1.3% Cr, and 6.5% Si, just before protoenstatite begins to form by reaction of forsterite with both the gas and the liquid. At 1537 K, plagioclase, $X_{Ab} = 0.056$, begins to form by reaction of gaseous Na with the liquid and, at 1527 K, the liquid disappears into a mixture of plagioclase and fassaite whose composition is $X_{CaTs} = 0.049$, $X_{T_3P} = 0.035$, and $X_{T_4P} = 0.016$. At 1400 K, X_{Fa} in olivine is 1.7×10^{-3}. At 1363 K, Ti_3O_5 is oxidized to Ti_4O_7. At 1233 K, Cr in the metal alloy reacts with plagioclase and magnesium silicates to form an $MgCr_2O_4$-rich spinel solid solution whose X_{Cr} and X_{Fe} are 0.87 and 0.012, respectively.

The pressure-temperature stability fields of vapor only, crystalline phases + vapor, and CMAS liquid + vapor in a gas of solar composition are summarized in Fig. 5. The position of the liquid field has been carefully determined by complete condensation calculations along fourteen different isobars between 1×10^{-2} and 100 atm, the details along only two of which, 0.3 atm and 1.5 atm, were discussed above. Note that two lobes in the liquid field extend to particularly low total pressure in two different temperature intervals, one extending from 1900 to 1800 K and the other from 1650 to 1520 K. The liquid in the high-temperature lobe is the low-MgO (<1%) one which crystallizes into gehlenite and $CaAl_4O_7$ at $P^{tot} = 0.3$ atm. The lower-temperature liquid contains high MgO, ~20%, and crystallizes into fassaite and anorthite at 0.1 atm. It is the latter liquid which establishes the minimum total pressure necessary for stabilizing any liquid in a gas of solar composition at $\sim 5 \times 10^{-2}$ atm. In the region above $P^{tot} = 1$ atm where the highest-temperature condensate is a liquid, the initial composition of the liquid is very rich in Al_2O_3 and CaO, but shifts from 47 mol% CaO, 51% Al_2O_3, and 2% SiO_2 at 10 atm to 54 mol% CaO, 2% MgO, 40% Al_2O_3, and 4% SiO_2 at $P^{tot} = 100$ atm. At P^{tot} above 0.2 atm, the lowest-temperature liquid disappears at progressively higher temperatures with increasing P^{tot}, but does not vary much in composition, containing ~17 mol% CaO, 21% MgO, 9% Al_2O_3, and 53% SiO_2.

4.4. Variation of Solution Compositions with Total Pressure

The variation of the liquid composition with temperature is shown at several different total pressures in Fig. 6. At $P^{tot} = 1.5$ atm, a liquid containing 58 mol% Al_2O_3, 41% CaO, and 1% SiO_2 is the highest-temperature condensate. As the temperature falls, more CaO condenses into the liquid, diluting the Al_2O_3. As the temperature continues to fall, the Al_2O_3 and CaO contents gradually fall as significant amounts of SiO_2 and then MgO begin to condense into the liquid. Superimposed upon these general trends are inflection points at temperatures at which various phases containing CaO, MgO, Al_2O_3, or SiO_2 become stable. The highest-temperature one, labelled c in Fig. 6, is for spinel, whose precipitation from the liquid causes the rate of decline of Al_2O_3 content with decreasing temperature to increase, temporarily decreasing the rate of decline of the CaO content with decreasing temperature. The next (j) is for forsterite, whose condensation causes the MgO content of the liquid to begin a monotonic decrease with falling temperature, braking the rate of decline of the CaO and Al_2O_3 contents. Below this temperature, spinel gradually dissolves in the liquid, increasing its Al_2O_3 content gradually, until the temperature is reached (l) at which spinel is exhausted, causing the Al_2O_3 content to fall with decreasing temperature until enstatite condenses (n). Below this temperature, the SiO_2 content of the liquid remains constant, and the continuous decrease in MgO content causes the CaO and Al_2O_3 contents to rise slightly. When anorthite becomes stable (k), the CaO content increases slightly and that of Al_2O_3 decreases slightly. At a slightly lower temperature, fassaite becomes stable (g) and the liquid disappears.

The curves showing the variation of the liquid composition with temperature at lower P^{tot} are almost the same as those at

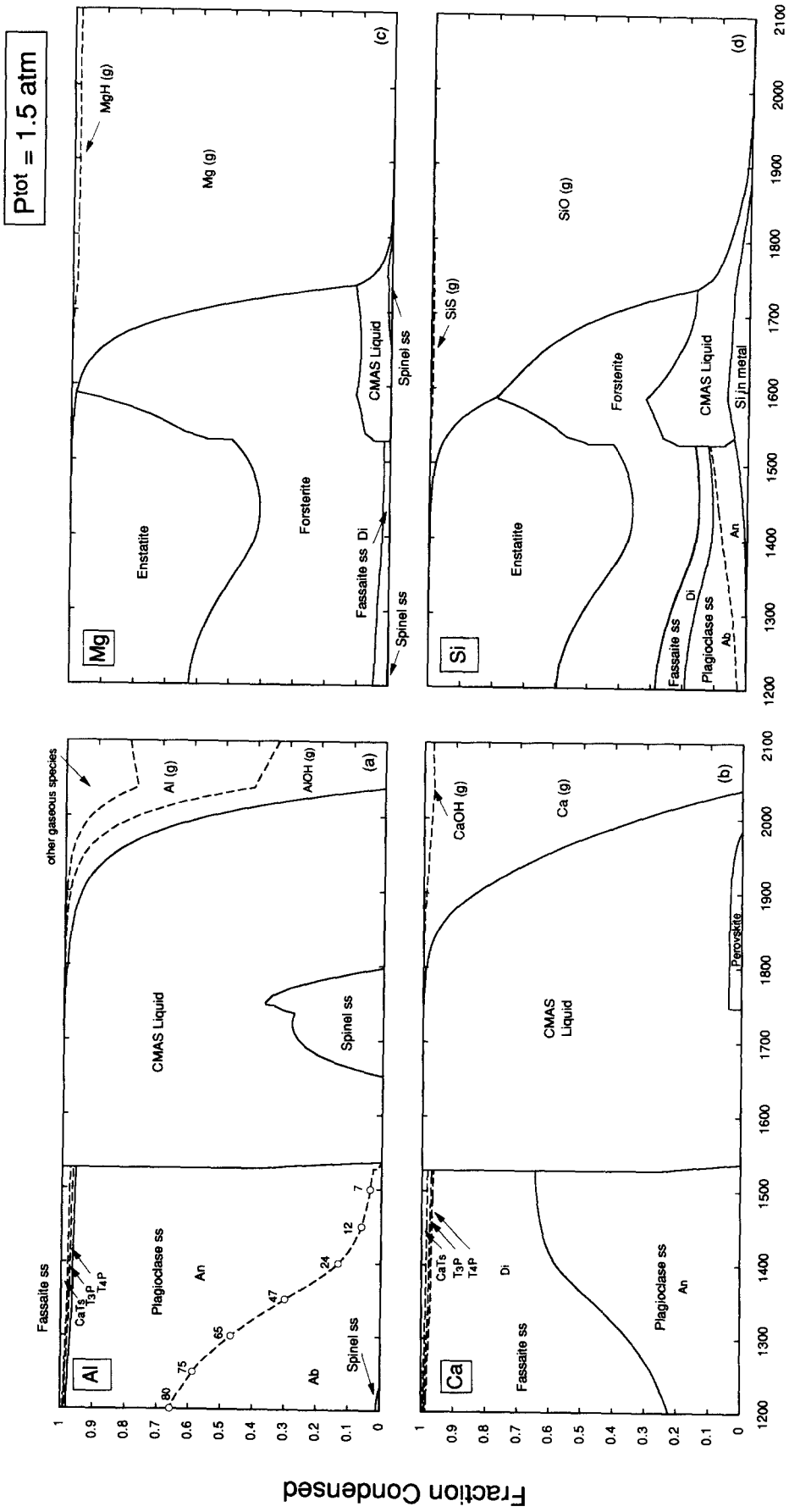

FIG. 4. The distribution of (a) Al, (b) Ca, (c) Mg, and (d) Si between condensed phases and vapor as a function of temperature in a solar gas at $P^{tot} = 1.5$ atm. Condensation occurs at such high temperatures at this total pressure that, with relatively minor exceptions, all of the Al and Ca are in the liquid over a 500 K temperature interval. Conventions and abbreviations as in previous figures.

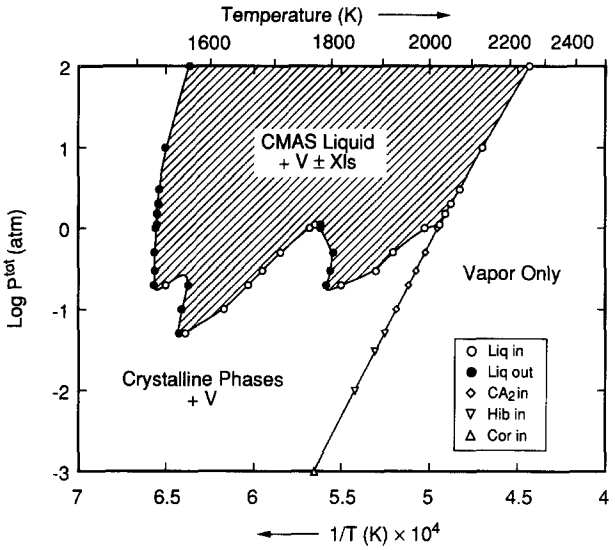

FIG. 5. The ranges of total pressure and temperature over which CMAS condensate liquids are stable in a system of solar composition. Liquid in and liquid out refer to the appearance and disappearance of liquid, respectively, upon isobaric cooling. Liq, liquid; V, vapor; Xls, crystalline phases. Other abbreviations as used previously.

1.5 atm except for a progressive shift of the equilibria to lower temperatures with decreasing total pressure, temperature gaps where liquids do not exist which widen with decreasing P^{tot}, and small changes in the relative temperatures of the inflection points as the sequence of appearance of solid phases with falling temperature changes slightly with decreasing P^{tot}. Examples of the latter at 1 atm are the break in the rate of fall of the Al_2O_3 content where melilite precipitates (b) at 1821 K, the crystallization of spinel at the temperature at which the liquid first disappears, and the complete melting of melilite (d) at the temperature at which the liquid reappears. At P^{tot} = 0.3 atm, the liquid first disappears when melilite, rather than spinel, crystallizes from it, with spinel forming in the absence of liquid at a temperature above that at which the liquid reappears. As P^{tot} falls, truncation of the increase in MgO content of the liquid with falling temperature by condensation of forsterite occurs at progressively lower MgO concentrations, causing the low-temperature parts of the MgO and CaO curves to come closer together until, at 0.1 atm, the CaO contents of the liquids are higher than the MgO contents.

These liquids are highly non-ideal. Using the liquids which form at 1 atm as examples, the activity coefficients for CaO, MgO, Al_2O_3, and SiO_2 are 3.3×10^{-3}, 0.21, 0.35, and 4.5×10^{-2}, respectively, relative to pure liquid oxides at 1991 K, the temperature of initial condensation of liquid. When the liquid disappears due to precipitation of spinel and melilite at 1781 K, the activity coefficients are 7.1×10^{-4}, 0.17, 0.27, and 0.11, respectively. They are 3.5×10^{-4}, 5.1×10^{-2}, 0.19, and 0.25, respectively, when forsterite condenses at 1717 K and 1.2×10^{-5}, 9.6×10^{-3}, 4.0×10^{-2}, and 1.01, respectively, when the liquid disappears due to precipitation of fassaite and plagioclase at 1526 K.

The variation of X_{Ak} in melilite with temperature is shown at different total pressures in Fig. 7. At all pressures, X_{Ak} is lowest in the highest-temperature melilite to form, rises steadily with falling temperature, and reaches a maximum at a temperature just above the temperature of melilite disappearance. In all cases, the maximum X_{Ak} reached increases with the width of the temperature interval for melilite stability. With increasing total pressure, the latter increases up to 0.1 atm and then decreases, the reversal being due to the fact that melilite disappears by reaction with the gas to form either fassaite or rankinite at $P^{tot} \leq 1 \times 10^{-2}$ atm but by a different mechanism, dissolution in condensate liquids, at higher pressures. As a result, the maximum X_{Ak} increases from 0.13 at 1 atm to 0.57 at 0.1 atm and then decreases to 0.16 at 1×10^{-6} atm. The flat top on the curve for 1×10^{-2} atm is due to the coincidental coexistence of both spinel and forsterite with melilite, making the X_{Ak}/X_{Gc} ratio of the latter almost constant over a small temperature range at this P^{tot}. The unusually large gap between the curves for 1×10^{-2} and 0.1 atm is due to our use of the thermodynamic data of Berman (1983) for åkermanite at $P^{tot} \geq 0.1$ atm, where liquids are stable, and of the data of Charlu et al. (1981) at lower pressures. The added stability of åkermanite in Berman's data shifts all the high-pressure curves higher by about 15 K.

The variation of the composition of high-temperature, Al-rich spinel with temperature is shown at different total pressures in Fig. 8b and d. The form of the variation of the molar Fe/Fe + Mg ratio with temperature is different at different total pressures, due entirely to the pressure-dependent variation of the relative condensation temperatures of the metal alloy, spinel, and forsterite. At $P^{tot} \geq 0.1$ atm, the ratio is a maximum at the initial formation temperature of spinel, falls rapidly with decreasing temperature as co-condensing metallic iron removes Fe from the gas, then increases gradually with decreasing temperature after forsterite condensation begins to remove significant Mg from the gas. With increasing P^{tot}, the fraction of the Fe already condensed as metal prior to spinel formation increases steadily, causing the initial molar Fe/Fe + Mg ratio in the spinel to fall from 1.7×10^{-3} at 0.1 atm to 1.1×10^{-3} at 1.5 atm. In this pressure range, the minimum and final molar Fe/Fe + Mg ratios are 3.7–4.5 $\times 10^{-4}$ and 5.6–6.3 $\times 10^{-4}$, respectively. At 1×10^{-2} and 1×10^{-3} atm, Al-rich spinel condenses at a higher temperature than metallic iron. The resulting curves are similar to those at higher pressures except for the addition of high-temperature segments in which the molar Fe/Fe + Mg ratios fall gradually with decreasing temperature due to formation of $MgAl_2O_4$ as a by-product of Mg enrichment of melilite. In the pressure range of 1×10^{-4} to 1×10^{-6} atm, the final Fe/Fe + Mg ratio is higher than the initial one. At high temperature, the ratio falls with decreasing temperature due to the melilite reaction, then rises after forsterite condensation begins to consume Mg. At 1×10^{-4} atm, forsterite and metallic iron condense at almost the same temperature, but iron condenses after forsterite at lower pressure. At 1×10^{-4} and 1×10^{-5} atm, the relative rate of condensation of Mg in forsterite is faster than that of Fe in the alloy, allowing the Fe/Fe + Mg ratio of coexisting spinel to continue to rise with falling temperature after metal alloy condensation. At 1×10^{-6} atm, spinel disappears prior to metallic iron condensation. The initial, minimum, and final molar Fe/Fe + Mg ratios vary from 6.0 $\times 10^{-4}$, 4.9×10^{-4}, and 7.1×10^{-4}, respectively, at 1

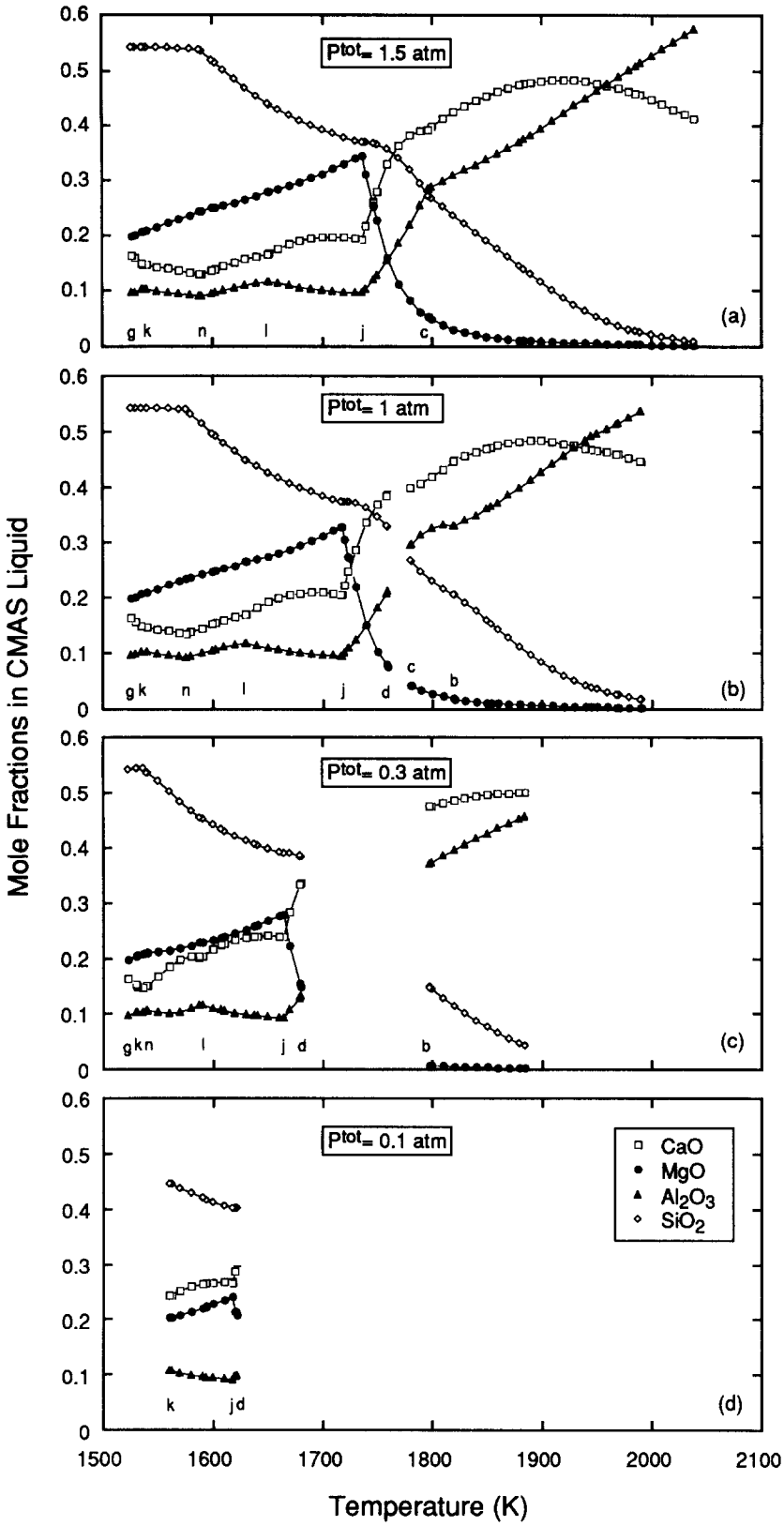

FIG. 6. The variation of the concentrations of CaO, MgO, Al_2O_3, and SiO_2 in condensate liquids with temperature in a solar gas at total pressures of (a) 1.5 atm, (b) 1 atm, (c) 0.3 atm, and (d) 0.1 atm. Note that liquid exists continuously over the entire temperature range of interest at 1.5 atm but that the temperature interval for the stability of liquid is interrupted by the solidus for ~20 K at 1 atm and ~120 K at 0.3 atm. Liquid is stable for only ~60 K at 0.1 atm. Inflection points on the curves are due to the onset of crystallization or disappearance of a coexisting phase at the temperature of the inflection, labelled as follows: b, melilite in; c, spinel in; d, melilite out, liquid in; g, fassaite in; j, forsterite in; k, anorthite in; l, spinel out; n, enstatite in. Abbreviations as used previously.

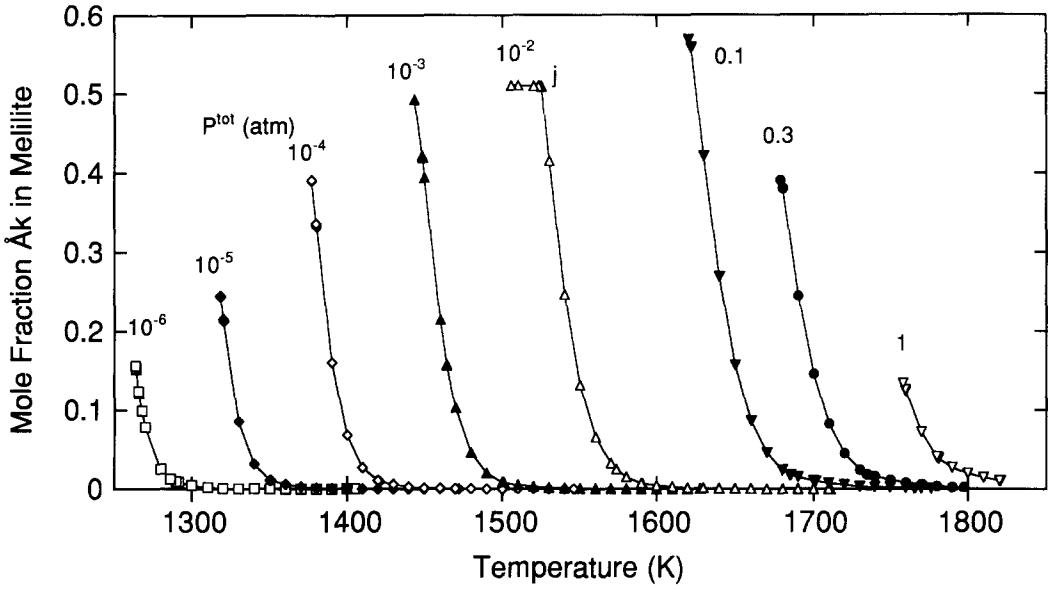

FIG. 7. The variation of mole fraction åkermanite in melilite with temperature in a solar gas at the total pressure indicated for each curve. Abbreviations and labels for inflection points as used previously.

$\times 10^{-4}$ atm to 2.6×10^{-4}, 2.2×10^{-4}, and 4.5×10^{-4}, respectively, at 1×10^{-6} atm.

At all total pressures, the Cr/Cr + Al ratio of Al-rich spinel is lowest at its initial condensation temperature, steadily increases with falling temperature, less steeply in temperature intervals where $MgAl_2O_4$ is being produced as a result of the varying composition of the fassaite and more steeply when $MgAl_2O_4$ is being consumed to form anorthite, and reaches its maximum at a temperature just above that at which spinel disappears. The minimum molar Cr/Cr + Al ratio rises from 2.7×10^{-4} at 1.5 atm total pressure to 7.6×10^{-4} at 1×10^{-6} atm, as does the maximum ratio from 1.7×10^{-3} to 1.8×10^{-2} at these respective pressures.

The composition variation of low-temperature, Cr-rich spinel is shown at different total pressures in Fig. 8a and c. The Al for this phase comes from consumption of a small amount of plagioclase, the Mg from small amounts of coexisting magnesium silicates, and the Cr and Fe from oxidation of the metal alloy. The formation temperature of this phase and its initial Fe/Fe + Mg and Cr/Cr + Al ratios increase from 1196 K, 6.9×10^{-3} and 0.67 at 1×10^{-5} atm total pressure to 1233 K, 1.2×10^{-2} and 0.87 at 1.5 atm. The Fe/Fe + Mg and Cr/Cr + Al ratios increase together with falling temperature, reaching 4.2×10^{-2} and 0.83, respectively, by 900 K at $P^{tot} = 1 \times 10^{-5}$ atm and 9.3×10^{-2} and 0.88, respectively, by this temperature at $P^{tot} = 1.5$ atm. These increases are monotonic, except for the Cr/Cr + Al ratio which, at $P^{tot} = 1.5$ atm, is almost constant and, at $P^{tot} = 1 \times 10^{-6}$ atm, begins at 0.66 at 1161 K, falls to 0.47 at 940 K, and rises to 0.63 by 900 K.

The dependences of X_{CaTs}, X_{T_3P}, X_{T_4P}, and the X_{T_3P}/X_{T_4P} ratio on temperature are shown at different total pressures in Fig. 9a,b,c, and d, respectively. The relative proportions of CaTs, T_4P, T_3P, and Di are discontinuous functions of temperature due to reactions involving other condensate phases containing the same elements as these components. The dependence of the concentration of each component on temperature is similar at all total pressures $\leq 1 \times 10^{-3}$ atm. In the temperature interval immediately below the initial condensation point of fassaite, perovskite is consumed to form T_3P and T_4P, and either melilite, or melilite + rankinite, or melilite + rankinite + anorthite, or rankinite + anorthite, depending on P^{tot}, are consumed in a reaction with gaseous Mg and Si to form spinel and more Di than CaTs. As a result, each of X_{CaTs}, X_{T_3P}, and X_{T_4P} falls steeply with decreasing temperature over this interval. After the above phases are consumed, CaTs and T_4P react with gaseous Mg and Si to form Di, spinel, and T_3P, causing X_{CaTs} to fall steeply, X_{T_3P} to rise, and X_{T_4P} to decline with decreasing temperature. Forsterite condensation then limits the availability of Mg and Si, drastically reducing the rate of decline of X_{CaTs} with decreasing temperature. CaTs, Di, and spinel then react with gaseous Si to form anorthite and forsterite, causing X_{CaTs} to fall and both X_{T_3P} and X_{T_4P} to rise with falling temperature. After spinel is consumed, gaseous Si reacts with CaTs and T_4P to produce anorthite + T_3P, causing X_{CaTs} to decline further along with X_{T_4P} while X_{T_3P} rises with falling temperature. X_{CaTs} continues to fall, X_{T_4P} falls more steeply, and X_{T_3P} begins to fall with declining temperature after either Ti_3O_5 or Ti_4O_7 or sphene ($CaTiSiO_5$) becomes stable. After condensation of enstatite, availability of gaseous Si becomes more limited, and the decline of each of X_{CaTs}, X_{T_3P}, and X_{T_4P} with falling temperature becomes less steep, although X_{T_3P} now falls more steeply than X_{T_4P}. At 1×10^{-2} atm, the sequence of reactions is the same, except that forsterite is present when fassaite first condenses, limiting the availability of Mg. In this case, immediately after fassaite condenses, the melilite reaction with gaseous Mg and Si produces spinel and more CaTs than Di, causing a gradual increase in X_{CaTs} with falling temperature at the high-temperature end of the curve. At $P^{tot} \geq 0.3$ atm, liquid is so stable that fassaite precipitation from it is delayed until a temperature below the condensation temperature of enstatite. The composition variation of the fassaite at this pressure is the same as at all other

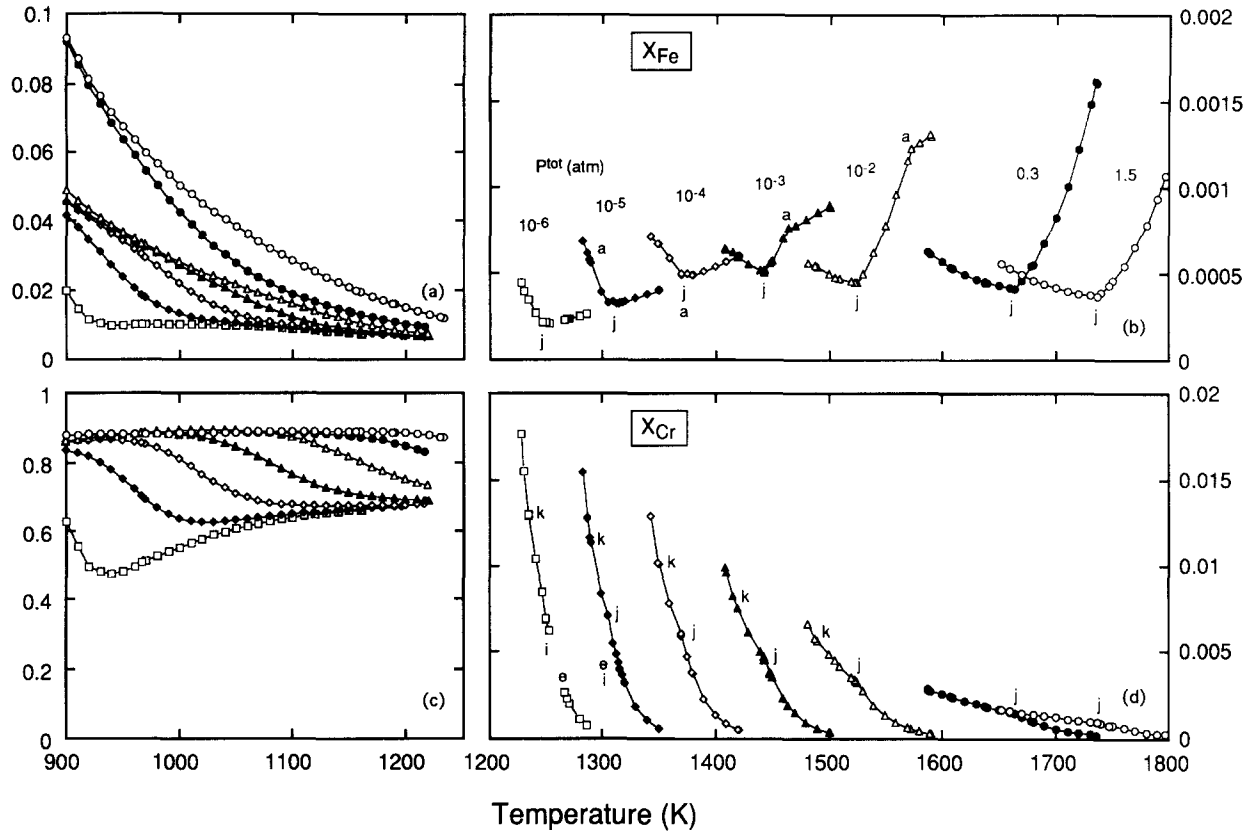

FIG. 8. The variation of (a, b) X_{Fe} and (c, d) X_{Cr} in (a, c) low-temperature, Cr-rich and (b, d) high-temperature, Al-rich spinel with temperature in a solar gas at the total pressures whose symbols are labelled in (b). Inflection points: a, metal alloy in; e, anorthite in, spinel out; i, spinel in, anorthite out. Abbreviations and labels for other inflection points as used previously.

total pressures below the temperature of enstatite formation, dominated by dilution of T_3P, T_4P, and CaTs with Di produced from the Ca released as the plagioclase becomes more albitic with falling temperature and from Mg and Si made available by conversion of enstatite to forsterite.

The atomic Ti^{3+}/Ti^{4+} ratio in fassaite is simply the ratio of mole fractions of T_3P to T_4P. Because of the above mineral reactions that occur during condensation, each of these mole fractions varies with temperature somewhat independently of the other. As a result, the atomic Ti^{3+}/Ti^{4+} of fassaite in equilibrium with a gas of solar composition varies irregularly with falling temperature, first rising gradually until spinel is consumed, then more steeply until enstatite condenses, then falling steadily, as shown in Fig. 9d. Also shown in this figure is the variation of P_{O_2} with temperature in the coexisting gas at three different total pressures. Because the P_{O_2} declines gradually with falling temperature, the atomic Ti^{3+}/Ti^{4+} ratio of fassaite is not a monotonic function of the P_{O_2}. It is important to note that curves for the variation of log P_{O_2} with temperature in the range of P^{tot} from 1×10^{-5} to 1×10^{-3} atm all lie within the envelope of the curves for the three different total pressures shown, and thus the variations of both P_{O_2} and P_O with P^{tot} are very small at any given temperature over this temperature range. This important exception to the general rule that partial pressures vary directly with P^{tot} is a consequence of the equilibrium $H_{2(g)} + {}^1/_2\ O_{2(g)} \rightleftarrows H_2O_{(g)}$ which requires P_{O_2}, and therefore P_O, to be a function of the ratio of P_{H_2O} to P_{H_2}, both of which vary directly with P^{tot}.

The variation of the plagioclase composition with temperature is shown at several different total pressures in Fig. 10. Because Na is much more volatile than Ca, X_{Ab} is lowest in the highest-temperature plagioclase to form but rises steadily, reaching a maximum of 0.82 approximately 450 K below the initial condensation temperature at all total pressures. This is the plagioclase composition that results when all of the Na forms albite and virtually all of the Al remaining after formation of albite and Cr-rich spinel is consumed by anorthite. X_{Ab} of the highest-temperature plagioclase rises steadily from 2.9×10^{-5} at 1×10^{-6} atm total pressure to 1.1×10^{-3} at 1×10^{-2} atm, jumping to 4.4×10^{-2} and 5.6×10^{-2} at 1 atm and 1.5 atm, respectively, where the existence of a liquid field delays plagioclase formation to lower temperatures than would otherwise be the case.

The variation with temperature of the metal alloy composition is shown at different total pressures in Fig. 11. At all total pressures, the Si content of the metal alloy rises steeply with falling temperature, less steeply after forsterite condensation begins to remove a significant amount of the Si from the gas and slightly more steeply again after exhaustion of spinel. The Si content reaches a maximum at the temperature immediately above the condensation temperature of enstatite, which removes virtually all of the remaining Si from the gas,

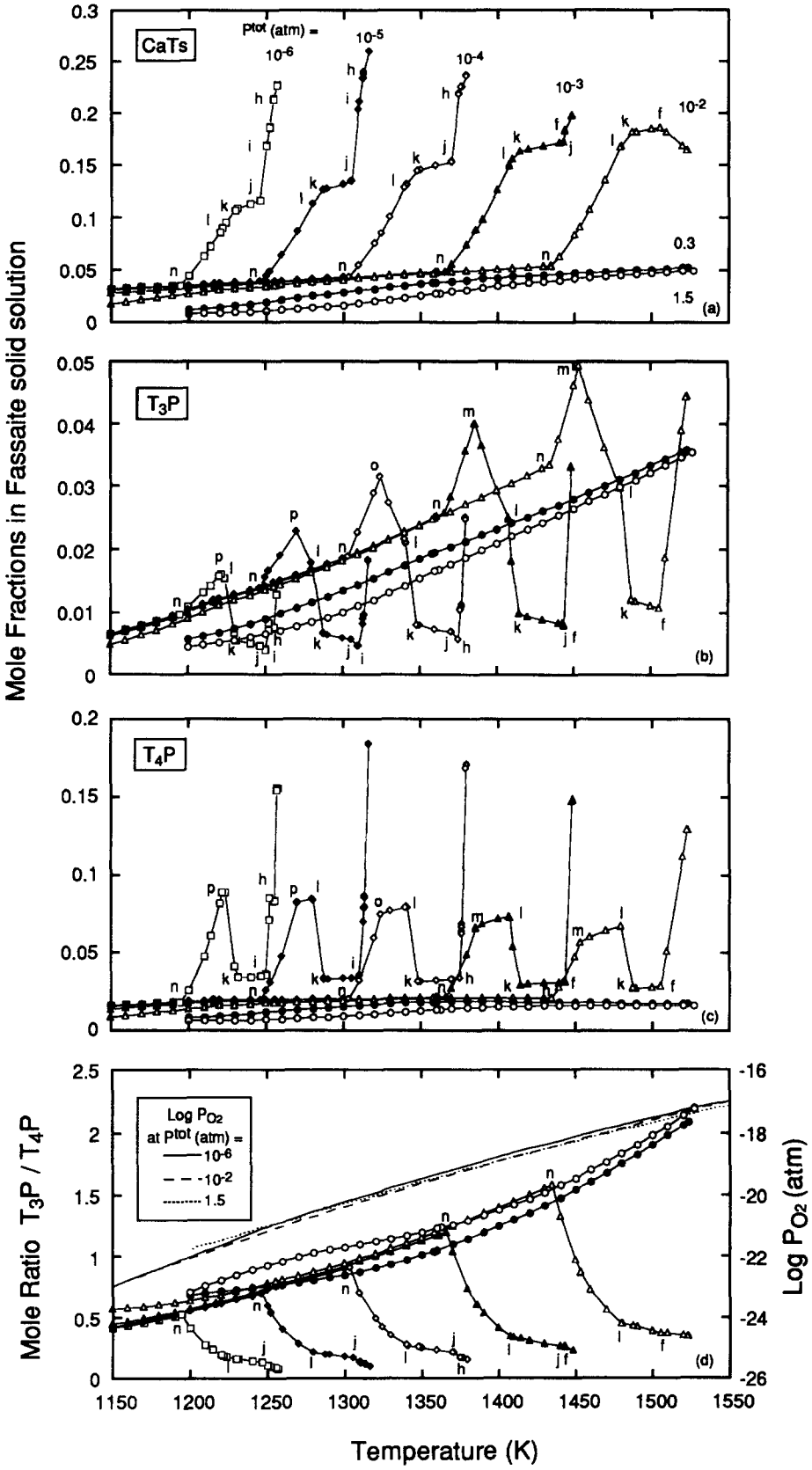

FIG. 9. The dependence of (a) X_{CaTs}, (b) X_{T_3P}, (c) X_{T_4P}, and (d) X_{T_3P}/X_{T_4P} in fassaite with temperature in a solar gas at the total pressures whose symbols are labelled in (a). The variation of log P_{O_2} with temperature at three different total pressures encompassing the range of total pressures of interest are shown for reference in (d). f, melilite out; h, rankinite out; m, Ti_3O_5 in; o, Ti_4O_7 in; p, sphene in. Abbreviations and labels for other inflection points as used previously.

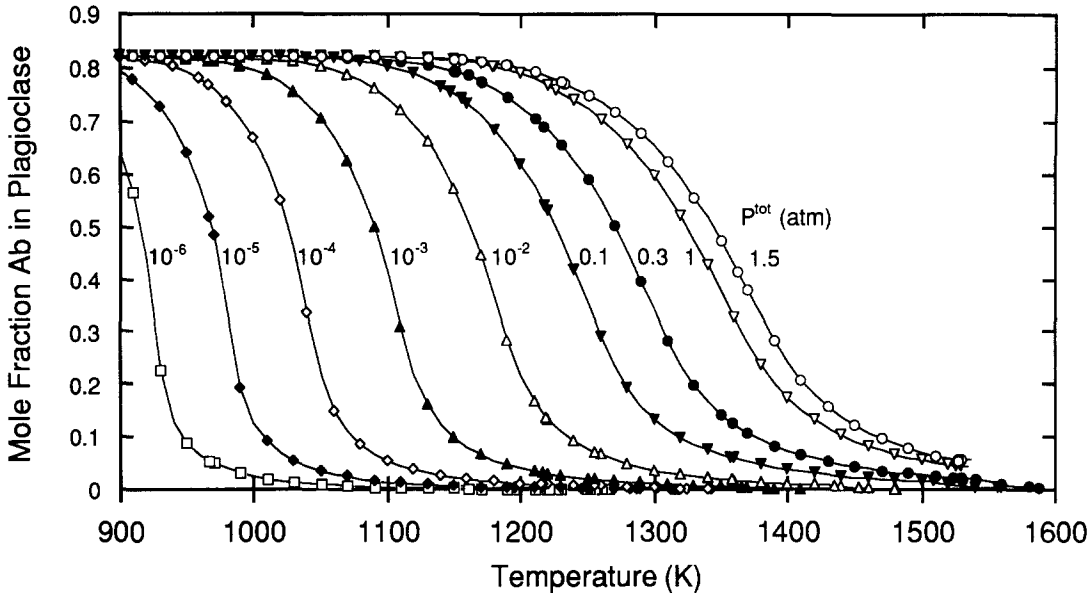

FIG. 10. The dependence of X_{Ab} in plagioclase with temperature in a solar gas at the total pressure indicated for each curve. Abbreviations as used previously.

causing the Si content of the metal alloy to fall to below 0.1 mol%. Both the initial and maximum Si contents increase progressively with increasing P^{tot}, from 1.3×10^{-2} and 1.8×10^{-2} mol%, respectively, at 1×10^{-6} atm to 2.0 and 6.5%, respectively, at 1.5 atm total pressure. The condensation curves for Ni and Co are steeper than that for Fe at all total pressures. As a result, the Ni and Co concentrations of the metal alloy are maxima at the initial condensation temperature of the alloy and fall off exponentially with decreasing temperature as they are diluted by Fe, eventually reaching levels corresponding to cosmic Ni/Fe and Co/Fe ratios when all three elements are totally condensed. At pressures of 1×10^{-2} atm and below, Ni and Co reach their minimum concentrations of 5.14 and 0.23 mol%, respectively, approximately 150 K below the initial condensation temperature of the alloy. Because of the much higher maximum Si contents in the alloy at higher pressures, however, Ni and Co levels are more dilute, and fall to slightly below the above concentrations before rising to them as the Si content gradually falls with declining temperature. Maximum Ni and Co contents fall from 33.1 and 0.65 mol% at 1×10^{-6} atm total pressure to 14.8 and 0.44%, respectively, at 1.5 atm. At all total pressures, the Cr condensation curve is less steep than that of Fe. As a result, the Cr content of the metal alloy increases gradually with decreasing temperature, more steeply in temperature intervals where $MgAl_2O_4$-consuming reactions occur. When Cr is totally condensed into an alloy with all of the Fe, Ni, and Co, the alloy contains 1.4 mol% Cr. At $P^{tot} \geq 1 \times 10^{-3}$ atm, this Cr content is reached by the alloy at a temperature above that for formation of Cr-spinel (q) but, at lower P^{tot}, the alloy has lower Cr contents at the temperature of Cr-spinel formation. The latter phase forms at the expense of metallic Cr, causing the concentration of Cr in the metal alloy to fall steeply with decreasing temperature below the initial condensation temperature of Cr-spinel, diminishing to below 0.1 mol% by 1090 K at all total pressures. At $P^{tot} = 1.5$ atm, the maximum Cr content of the alloy occurs at ~400 K below the condensation temperature of the alloy whose initial Cr content is 0.32 mol%. At $P^{tot} = 1 \times 10^{-6}$ atm, the initial Cr content of the alloy is 7.9×10^{-2} mol% but the maximum is only 0.36 mol%, as the increase in Cr content with falling temperature is truncated by formation of Cr-spinel at 1161 K, only 53 K below the alloy condensation temperature.

5. CONDENSATION AT ENHANCED DUST/GAS RATIOS

Cl chondrites have much higher ratios of oxygen and nonvolatile elements to hydrogen than does the sun. This is in accord with condensation calculations which show that, during condensation of a gas of solar composition, the nonvolatile elements are totally condensed, oxygen is ~20% condensed and hydrogen virtually uncondensed at the equilibration temperature of Cl chondrites. If the solar nebula formed by gravitational collapse of an interstellar gas cloud in which most of the condensable elements were present initially in previously formed circumstellar grains, it is easy to imagine that the ratios of oxygen to hydrogen and of nonvolatile elements such as Al and Mg to hydrogen in the total grain population were higher and those of the gas lower than their respective solar values. If these grains were able to concentrate in certain regions, such as the median plane of the disc, relative to the gas before those regions reached grain evaporation temperatures, then, upon evaporation of the grains, large gaseous regions could have formed in which the ratios of oxygen and condensable elements to hydrogen were considerably higher than the solar ratios. Such a scenario was first envisioned by Wood (1967) and was used by Fegley and Palme (1985), for example, in order to provide a nebular setting for condensation under more oxidizing conditions than those of a gas of solar composition. In that work, the dust/gas ratio was increased by factors of 50–500 relative to solar proportions in order to account for depletions of W and Mo relative to other siderophiles.

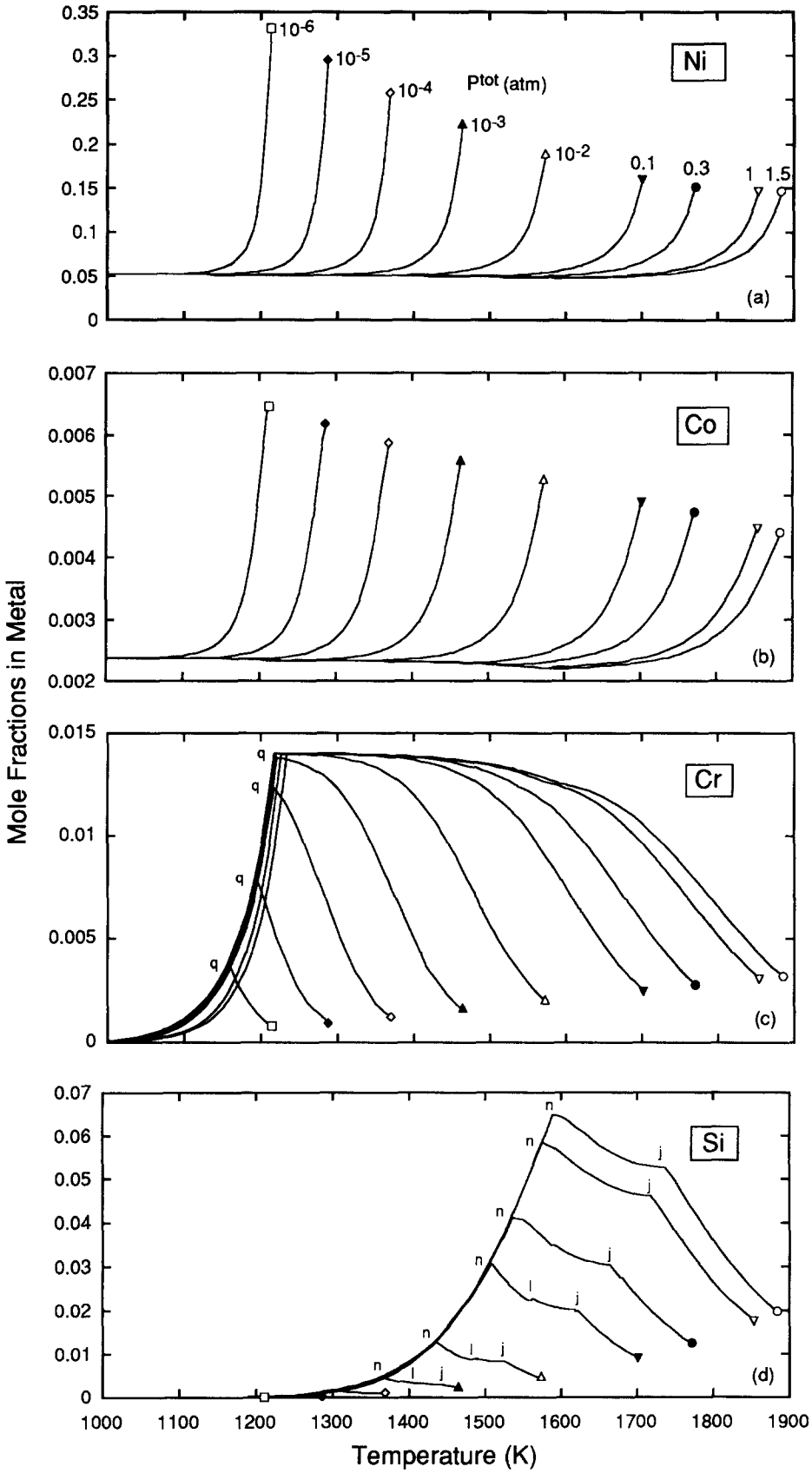

FIG. 11. The dependence of (a) X_{Ni}, (b) X_{Co}, (c) X_{Cr}, and (d) X_{Si} in the metal alloy with temperature in a solar gas at the total pressures whose symbols are labelled in (a). q, Cr-spinel in. Abbreviations and labels for other inflection points as used previously.

Just as enhancement of the dust/gas ratio has the desired effect of increasing P_{O_2} in the resulting vapor, it also increases the partial pressures of all of the condensable elements compared to their values in a gas of solar composition at the same total pressure. What was not appreciated by Fegley and Palme (1985) is that, if the dust/gas enrichment factor relative to the solar ratio is increased by as much as they envisioned, this phenomenon will result in condensation of partial melts even at low total pressure. This behavior was first explored by Wood and McSween (1977). Bartholomay and Larimer (1982) and Larimer and Bartholomay (1983) calculated the stability field of liquid and showed that an Al–Ca–Ti–rich silicate melt would be the first condensate at 1×10^{-3} atm if the dust, composed of the more refractory elements and their associated oxygen, were enriched by factors of 20–25 relative to solar abundances. A hint of this was also seen in the calculated results of Wood and Hashimoto (1993) in which fields of liquid of unspecified composition were found at a total pressure of only 10^{-5} bar when the dust, consisting of all of the troilite (FeS) and all of the elements that would be condensed with it in a system of solar composition, is enriched relative to the remaining gas by factors of 10^3 and 10^7 relative to solar composition. Both Bartholomay and Larimer (1982) and Wood and Hashimoto (1993) used ideal solution models for the liquids which appear during condensation. Because these liquids are in reality highly non-ideal, as we have shown above, the liquid stability fields found by Bartholomay and Larimer (1982) and Wood and Hashimoto (1993) must be regarded as highly uncertain. Specifically, because the activity coefficients of all of the components of the calculated condensate liquids are less than one relative to liquid oxides, these workers have actually underestimated the stabilities, and thus the condensation temperatures, of liquid condensates and have overestimated the minimum dust/gas ratios necessary to produce them.

In order to show that increasing the dust/gas ratio at low total pressure is just as effective in producing stable liquid condensates as is increasing the total pressure in a gas of solar composition, we held P^{tot} at 1×10^{-3} atm and performed complete condensation calculations at fourteen different fractionated compositions corresponding to dust/gas enrichment factors ranging from 5 to 10^3 relative to the solar abundances. The fields of vapor only, crystalline phases + vapor, and CMAS liquid + vapor so calculated are plotted in Fig. 12 as a function of dust/gas enrichment factor. This figure clearly shows extensive fields of stable liquid condensates at $P^{tot} = 1 \times 10^{-3}$ atm over temperature intervals which become broader and more continuous with increasing dust/gas ratio. The minimum dust/gas enrichment factor needed to stabilize a liquid condensate of any composition at $P^{tot} = 1 \times 10^{-3}$ atm is only 16 relative to the solar abundances, quite modest in comparison to the fractionations envisioned by Fegley and Palme (1985) and Wood and Hashimoto (1993). The shape of the liquid field in Fig. 12 is remarkably similar to that in Fig. 5. They are not identical, however, due to the fact that increasing the total pressure does not change the composition of the system, while increasing the dust/gas ratio at constant total pressure does. The latter change not only concentrates oxygen and the nonvolatile elements relative to H, a diluent, causing a general increase in all condensation temperatures,

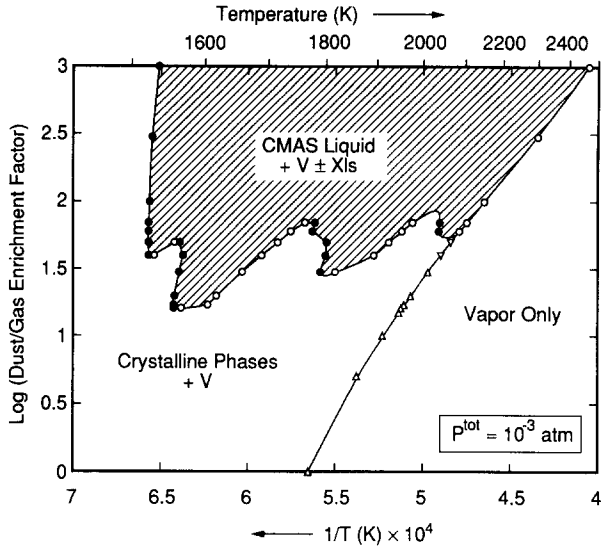

FIG. 12. Liquid-solid-vapor stability relations as a function of temperature and dust/gas enrichment factor at a total pressure of 1×10^{-3} atm. Symbols as in Fig. 5 and abbreviations as used previously.

but also fractionates the nonvolatile elements from oxygen, accentuating differential condensation temperature increases for phases with different cation/oxygen ratios.

Nevertheless, the sequence of condensation of oxygen-bearing solids and liquids and the detailed structures of the condensation diagrams are very similar regardless of whether liquid stability is achieved by increasing P^{tot} or the dust/gas ratio. Compare, for example, the distributions of Al, Ca, Mg, and Si between condensed phases and vapor at 1×10^{-3} atm total pressure and a dust/gas ratio 54 times that of a system of solar composition in Fig. 13a,b,c, and d, respectively, with those in a solar gas at $P^{tot} = 0.3$ atm seen in Fig. 3a,b,c, and d, respectively. The differences between these condensation sequences are relatively subtle. In the high dust/gas ratio case compared to the elevated pressure case, a hibonite field exists for 44 K prior to formation of $CaAl_4O_7$; the latter phase dissolves completely, instead of partially, into the CMAS liquid; after $CaAl_4O_7$ reprecipitates from the liquid, it persists for only 31 K, instead of 63 K; and melilite reaches an Åk content of only 24 mol%, instead of 39%, before disappearing. The temperatures of appearance and disappearance of both liquid and melilite and the variation with temperature of the composition of both liquid and melilite in the enhanced dust/gas ratio case are almost identical to those seen at $P^{tot} = 0.6$ atm. Similarly, the variation of X_{Ab} in plagioclase with temperature is almost identical to that at $P^{tot} = 0.1$ atm, and the temperature of condensation of metal and the variation of its Ni content with temperature are almost identical to those at $P^{tot} = 5 \times 10^{-2}$ atm.

Much more significant differences between the two situations are found in log P_{O_2} and in the effect of the latter upon the compositions of solid solution phases. The temperature of disappearance of Al-rich spinel, 1589 K, and the temperatures of appearance of protoenstatite, 1535 K, and fassaite, 1522 K, are virtually the same in the elevated pressure case and in the enhanced dust/gas ratio case. At these temperatures, log P_{O_2}

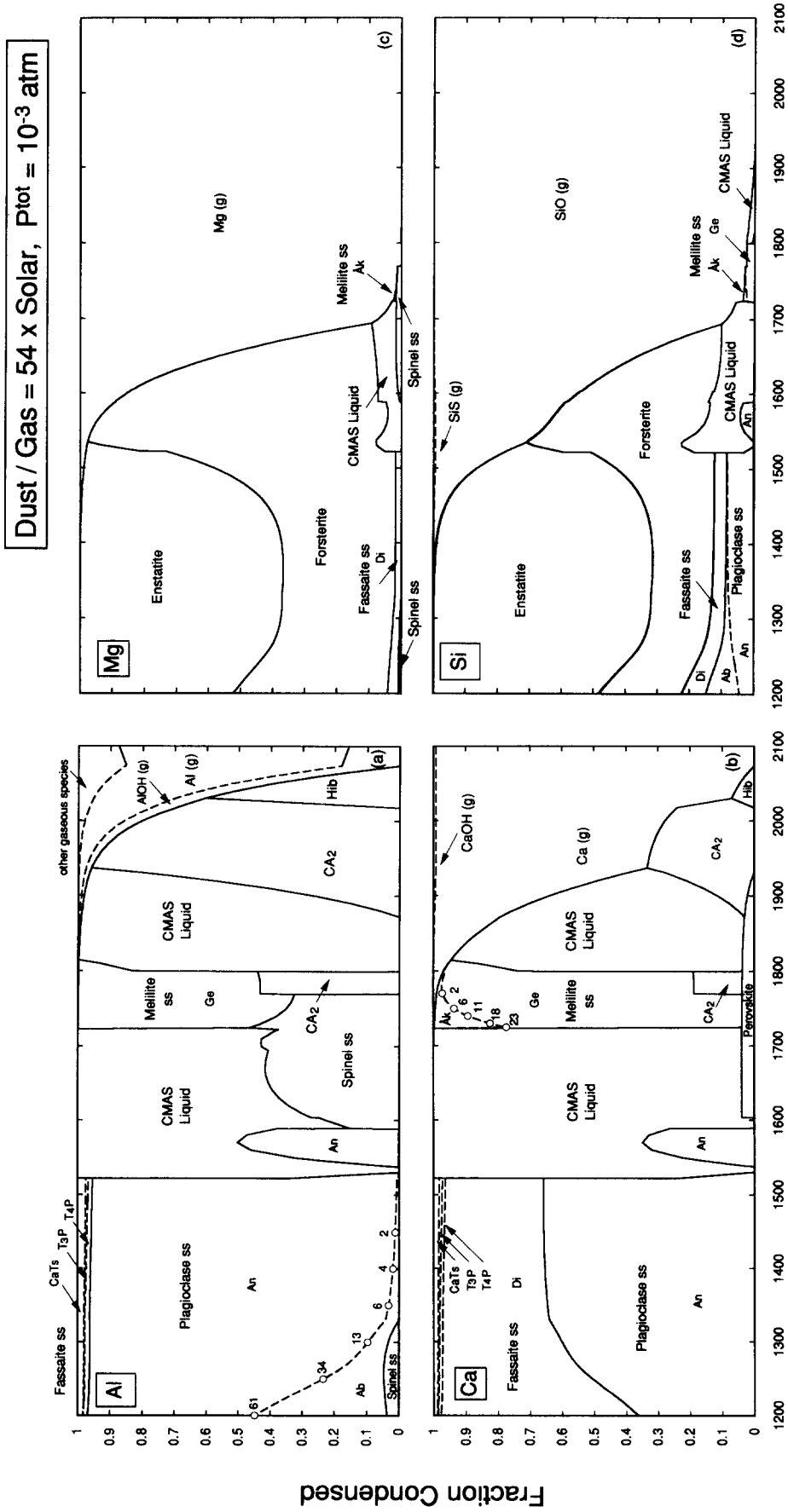

FIG. 13. The distribution of (a) Al, (b) Ca, (c) Mg, and (d) Si between condensed phases and vapor at a total pressure of 1×10^{-3} atm in a system enriched in dust relative to gas by a factor of 54 relative to their proportions in a system of solar composition (see text). Note the similarity in temperatures and structure between these figures and Figs. 3a,b,c, and d. The only significant differences are the appearance of a high-temperature hibonite field in the enhanced dust/gas ratio case and the relatively large fraction of the total Si accounted for by the metal alloy in the high-pressure case. Hib, hibonite. Conventions and other abbreviations as in previous figures.

is −16.7, −17.3, and −17.4, respectively, in the elevated pressure case but significantly higher, −15.2, −16.0, and −16.2, respectively, in the enhanced dust/gas ratio case. During condensation, Cr is partitioned between Al-rich spinel and the metal alloy and the Cr concentrations in both phases increase continuously with falling temperature, the molar Cr/Cr + Al ratio of spinel reaching a maximum at the temperature just above that of spinel disappearance. This ratio is 2.8 $\times 10^{-3}$, and X_{Cr} in the coexisting metal is 1.1×10^{-2} in the elevated pressure case but, because of the significantly higher P_{O_2}, the molar Cr/Cr + Al ratio in spinel is much higher, 2.2 $\times 10^{-2}$, and X_{Cr} in the metal lower, 6.1×10^{-3}, at this temperature in the enhanced dust/gas ratio case. For the same reason, the Fe/Fe + Mg ratio in spinel lies between 2.5 $\times 10^{-3}$ and 3.8×10^{-3} over the entire temperature interval for the stability of Al-spinel in the enhanced dust/gas ratio case, about twice as high as the maximum Fe/Fe + Mg ratio in Al-spinel in the elevated pressure case. The metal alloy always reaches its maximum Si content just above the condensation temperature of protoenstatite. At this temperature, the maximum Si content of the metal is 4.1 mol% in the elevated pressure case but, again because of the higher P_{O_2}, only 0.31% in the enhanced dust/gas ratio case. In addition, the Ti^{3+}/Ti^{4+} ratio in fassaite is highest in the highest-temperature fassaite to form, and gradually falls with decreasing temperature. In the elevated pressure case, the maximum Ti^{3+}/Ti^{4+} ratio is 2.08 and falls to 1.90 at 1500 K, 1.24 at 1400 K, and 0.85 at 1300 K. In the enhanced dust/gas ratio case, while the variation of X_{CaTs} with temperature is very similar to that in the elevated pressure case, Ti in the fassaite is more oxidized, with the maximum Ti^{3+}/Ti^{4+} being 1.00 and falling to 0.96 at 1500 K, 0.68 at 1400 K, and 0.44 at 1300 K.

Another significant difference between the elevated pressure case and the enhanced dust/gas ratio case is in the relative condensation temperatures of the metallic iron alloy and silicates such as forsterite. In raising the total pressure from 1×10^{-3} to 0.3 atm, thereby increasing P_{Fe} by a factor of 300, the condensation temperature of the alloy increases by 307 K, to 1771 K. At a constant total pressure of 1×10^{-3} atm, enhancing the dust/gas ratio by a factor of 54 also increases P_{Fe} by a factor of 54, causing the condensation temperature of Fe to increase by only 200 K, to 1664 K. The condensation temperature of forsterite, however, is a function of $P^2_{Mg}P_{Si}P^4_O$. Increasing the total pressure by a factor of 300 increases each of P_{Mg} and P_{Si} by about that factor, while P_O remains constant, as noted above, causing an increase in the forsterite condensation temperature of 221 K, to 1664 K, relative to its value at 1×10^{-3} atm total pressure. Enhancement of the dust/gas ratio by a factor of 54 at a constant P^{tot} of 1 $\times 10^{-3}$ atm causes an increase in P_{Mg} by about the same factor and an increase in P_{Si} by an even smaller factor due to formation of more $SiO_{(g)}$. Although this would appear to lead to a smaller increase in the forsterite condensation temperature than increasing P^{tot} to 0.3 atm, the opposite is true. The condensation temperature of forsterite increases by 251 K, to 1694 K, so that it actually condenses at a higher temperature than metallic iron in the enhanced dust/gas ratio case. This is because the forsterite condensation temperature depends on the fourth power of P_O and this parameter increases by a large factor in this case, despite the fact that the enrichment of oxygen in the dust is not as great as that of the nonvolatile elements compared to the solar abundances.

6. COMPARISON OF CALCULATED AND OBSERVED LIQUID-CRYSTAL PHASE RELATIONS

In all of our calculations, the highest-temperature liquids to condense are very low in MgO and SiO_2. For these, the agreement between calculated and experimentally determined liquid-crystal phase relations can be assessed using the Al_2O_3-rich portion of the phase diagram for the binary system $CaO-Al_2O_3$, illustrated in Fig. 14. Although two different experimental determinations of the phase relations exist, the discrepancies between them are small in the region of interest. In the ensuing discussion, bulk compositions are calculated on a perovskite-free basis. At $P^{tot} = 1.5$ atm, our calculations predict that no crystalline phases coexist with the liquid from its initial condensation temperature until below the temperature at which the liquid reaches such a high SiO_2 content, 5 wt%, that it is no longer in the $CaO-Al_2O_3$ binary. Over the temperature interval where the SiO_2 content is low, the calculated liquid compositions plot above the liquidus at their calculated equilibrium temperatures, in agreement with the experimentally determined phase diagram. At $P^{tot} = 0.1$ atm, the bulk composition of the condensate lies in the $CaO-Al_2O_3$ binary from the initial condensation temperature until melilite becomes stable at 1776 K. Over this temperature range, no liquids are predicted to be stable and, in agreement with the phase diagram, the trajectory of the condensate composition does not enter any liquid-containing field. When $CaAl_4O_7$ reacts with the gas at 1991 K to form the highest-temperature liquid at $P^{tot} = 1$ atm, the bulk composition of the condensate is seen to move into the $CaAl_4O_7$ + liquid field but the composition of the coexisting liquid is too poor in Al_2O_3 by ~2 wt% for it to plot on the liquidus. Alternatively, this discrepancy can be regarded as an error in the calculated liquidus temperature of ~25 K. On the other hand, the liquid is not exactly in the binary system, as it is predicted to contain 1.2 wt% SiO_2 at this temperature. As the temperature falls and the bulk composition of the condensate moves closer to the liquidus across the $CaAl_4O_7$ + liquid field, the discrepancy in Al_2O_3 content or liquidus temperature persists and becomes larger as the SiO_2 content of the liquid climbs to 4.6 wt%. Because of this, the bulk composition actually plots in the liquid-only field for ~15 K prior to the calculated disappearance temperature of $CaAl_4O_7$.

At $P^{tot} = 0.3$ atm, even the highest-temperature liquids contain 3.3 wt% SiO_2. Therefore, predictions of condensation calculations at this P^{tot} are best compared with the liquid-crystal phase relations in the $CaO-Al_2O_3-SiO_2$ ternary (Fig. 15) despite the fact that temperature resolution in the ternary is poorer than in the binary. The agreement is actually quite good. After $CaAl_4O_7$ reacts with the gas to form the highest-temperature liquid at 1885 K, the bulk composition of the condensate becomes progressively more CaO- and SiO_2-rich with falling temperature. Although the earliest liquids plot on isotherms which are about 30 K lower than the calculated temperatures and have compositions that plot slightly inside the $CaAl_2O_4$ + liquid field when the calculated phase assem-

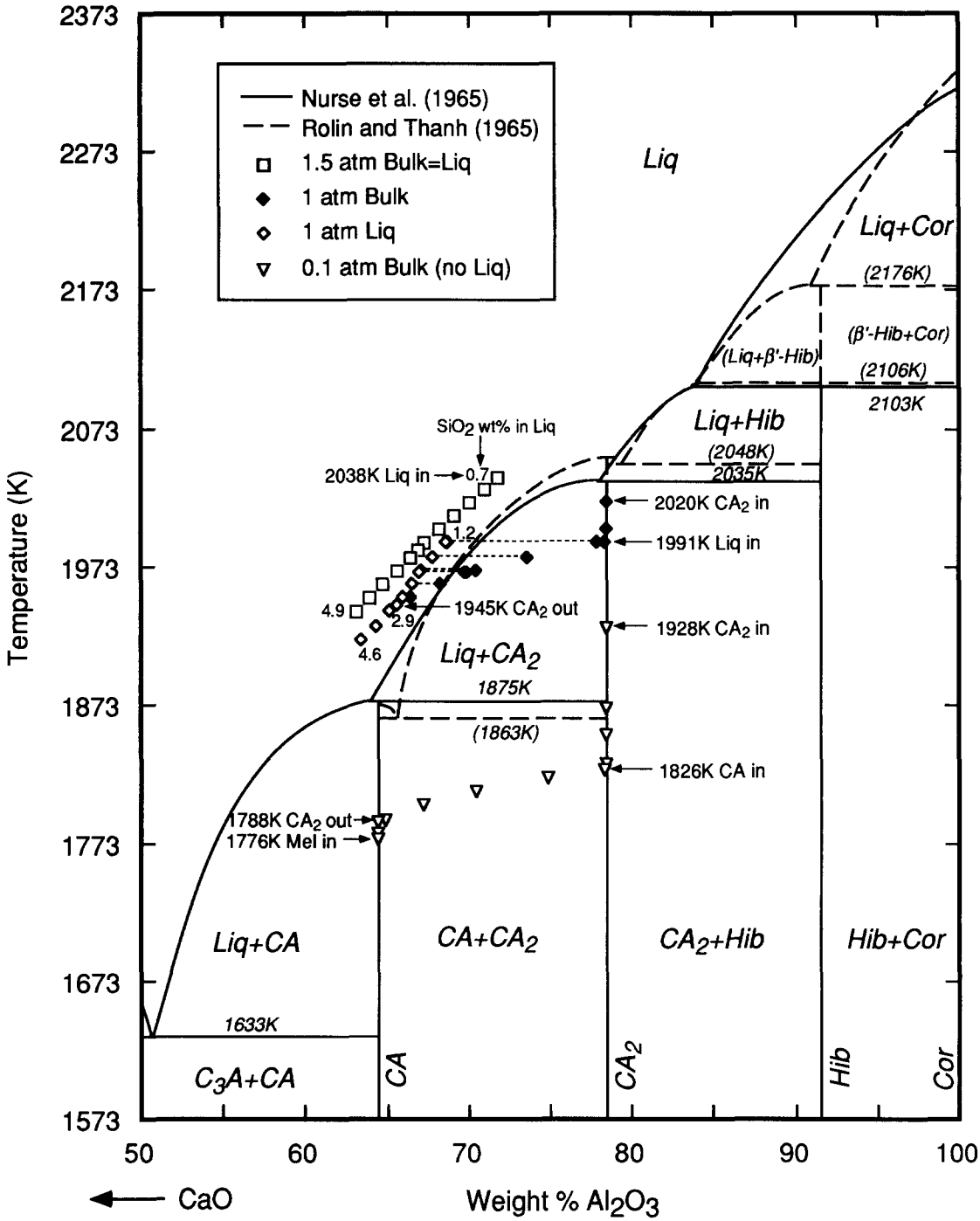

FIG. 14. Calculated composition-temperature trajectories of high-temperature, CaO-, Al_2O_3-rich bulk condensates and the liquid fractions of those condensates compared to two determinations of the crystal-liquid phase relations in the CaO–Al_2O_3 binary. Events calculated to occur at specific temperatures are marked along the trajectories. Each dotted line connects the compositions of a liquid with the bulk composition of the condensate assemblage of which it is calculated to be a part. Parentheses enclose labels of phase fields and temperatures found by Rolin and Thanh (1965). C_3A, $Ca_3Al_2O_6$. Other abbreviations as used previously.

blage is $CaAl_4O_7$ + liquid, the calculated liquid compositions move into the $CaAl_4O_7$ + liquid field and appear to plot much closer to the proper isotherms as the temperature falls below 1860 K. Furthermore, the calculated liquid composition is on the gehlenite + $CaAl_4O_7$ cotectic at approximately the correct temperature when these phases are predicted to co-crystallize from the condensate liquid.

In order to compare the phases predicted to be in equilibrium with more evolved condensate liquids to the phases observed experimentally to be in equilibrium with liquids of the

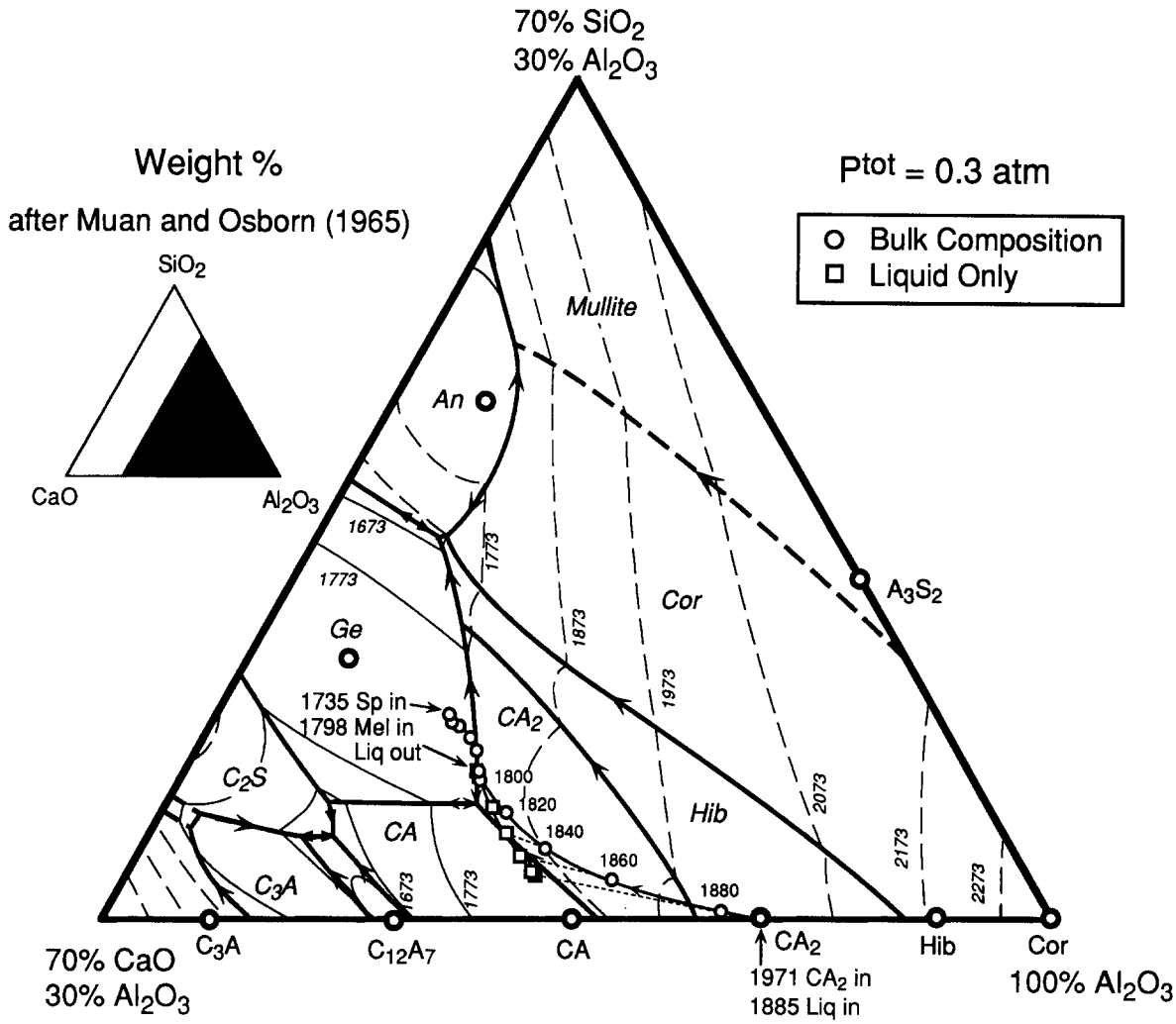

FIG. 15. Calculated composition-temperature trajectories of high-temperature, MgO-poor bulk condensates and the liquid fractions of those condensates at $P^{tot} = 0.3$ atm compared to the crystal-liquid phase relations in a portion of the CaO–Al_2O_3–SiO_2 ternary. Bold curves are boundaries of phase fields and bold open circles are compositions of pure phases. Less certain field boundaries and isotherms are dashed. A_3S_2, $3Al_2O_3 \cdot 2SiO_2$; $C_{12}A_7$, $12CaO \cdot 7Al_2O_3$; C_2S, Ca_2SiO_4. Other abbreviations and conventions as used previously.

same compositions, the composition trajectories of the bulk condensate and of the liquid fraction of the condensate at 0.3 atm and 0.1 atm are superimposed, in Figs. 16 and 17, respectively, on the liquid-crystal phase relations in a subsystem of CMAS projected from $MgAl_2O_4$ spinel onto the gehlenite-anorthite-forsterite plane. Comparisons of calculated equilibration temperatures of solid phase assemblages and condensate liquids with experimentally determined equilibration temperatures of the same solid phase assemblages and liquids of the same compositions are given in Figs. 18 and 19 for total pressures of 0.3 and 0.1 atm, respectively. In Figs. 16 and 17, the fields are labelled with the mineral phases which are in equilibrium with liquids having compositions which lie within the fields at the temperatures given by the isotherms. Immediately below 1680 K, the temperature at which spinel + melilite begin to react with the vapor to form liquid at 0.3 atm, the calculated liquid composition indeed plots within the spinel + melilite field (Fig. 16), but the calculated equilibration temperature is ~100 K above the observed equilibration temperature for that liquid (Fig. 18). After melilite dissolves completely in the liquid at 1678 K, spinel is the only phase calculated to be in equilibrium with it. Accordingly, the liquid compositions between 1678 and 1664 K plot well above the isotherms at which spinel and either melilite or forsterite would be in equilibrium with them. Forsterite is calculated to become stable at 1664 K, and forsterite + spinel to be in equilibrium with condensate liquids from 1664 to 1588 K. The calculated liquid composition at 1664 K indeed plots within 10 K of the isotherm where spinel + forsterite would be in equilibrium with it, and all of the calculated liquid compositions between 1664 and 1588 K plot within the spinel + forsterite field (Fig. 16) and have calculated temperatures of equilibration with spinel + forsterite that are within 25 K of the observed isotherms. Anorthite is calculated to join spinel + forsterite as a stable phase in equilibrium with condensate liquid at 1588 K. Accordingly, the calculated liquid composition is seen to cross into the spinel + anorthite field at a temperature just above the 1573 K isotherm. Because spinel

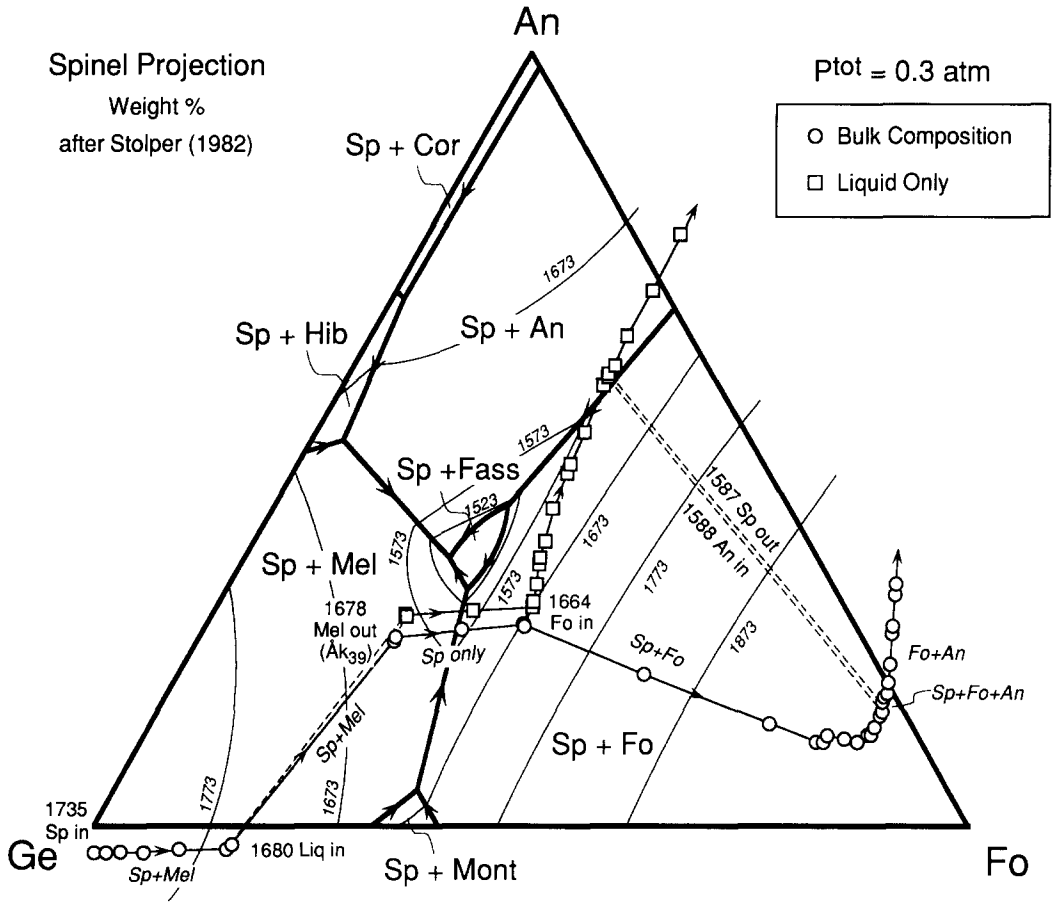

FIG. 16. Calculated composition-temperature trajectories of bulk condensates and their liquid fractions at P^{tot} = 0.3 atm superimposed upon the crystal-liquid phase relations in a portion of the CMAS system projected from $MgAl_2O_4$ spinel onto the gehlenite-anorthite-forsterite plane. Tie lines connecting compositions of bulk condensates with their liquid fractions are drawn for only a few temperatures. Each segment of the composition trajectory of the bulk condensates is labelled with the mineral assemblage, excluding perovskite, calculated to be stable over the temperature interval of the segment. Phase fields are labelled with the mineral assemblages that would be in equilibrium with liquids whose compositions plot within the fields at the temperatures given by the isotherms. Mont, monticellite. Other abbreviations and conventions as used previously.

disappears from the condensate assemblage at 1587 K, this phase diagram cannot be used for comparison with the calculations below this temperature.

At P^{tot} = 0.1 atm, melilite + spinel are again calculated to be in equilibrium with a liquid at a temperature ~ 100 K above the observed equilibrium temperature for that liquid (Fig. 17). Again, when melilite dissolves completely in the liquid and spinel is the only phase calculated to be in equilibrium with it, the calculated liquids exist at temperatures well above the isotherms for liquid + spinel + either melilite or forsterite (Fig. 17) until 1617 K when forsterite is calculated to join spinel and liquid. From 1617 until 1594 K, calculated spinel + forsterite + liquid equilibration temperatures are within 20 K of the observed isotherms. Fassaite is predicted to become stable at 1594 K, and spinel + forsterite + fassaite to be in equilibrium with condensate liquids over the temperature interval 1594 to 1562 K. Although the liquid compositions predicted in this temperature interval have equilibration temperatures which appear to plot very close to the observed isotherms for spinel + forsterite + liquid equilibrium, the compositions themselves plot just to the forsterite-rich side of the spinel + fassaite field (Fig. 17). When the calculated equilibration temperatures of those liquids are compared to those of the liquids closest in composition which are observed to be in equilibrium with spinel + forsterite + fassaite, however, the temperature discrepancy is seen to be 50–80 K (Fig. 19). At 1562 K, anorthite is predicted to become stable, joining spinel + forsterite + fassaite + liquid. Accordingly, the liquid composition calculated to be in equilibrium with the anorthite-containing assemblage plots on the spinel-anorthite-forsterite cotectic at about the correct isotherm (Fig. 17), but still ~50 K higher than the equilibration temperature of the nearest liquid composition observed to be in equilibrium with fassaite (Fig. 19), that composition being the quaternary invariant point at 1517 K (Yang et al., 1972; Treiman, 1990).

At temperatures below that at which anorthite replaces spinel in the condensate assemblage, the comparison between calculated and observed phase assemblages is best made by referring to the liquid-crystal phase relations in a subsystem of CMAS projected from forsterite onto the enstatite-anorthite-wollastonite ($CaSiO_3$) plane illustrated in Fig. 20. At P^{tot} = 0.3 atm, disappearance of spinel at 1587 K leaves an equi-

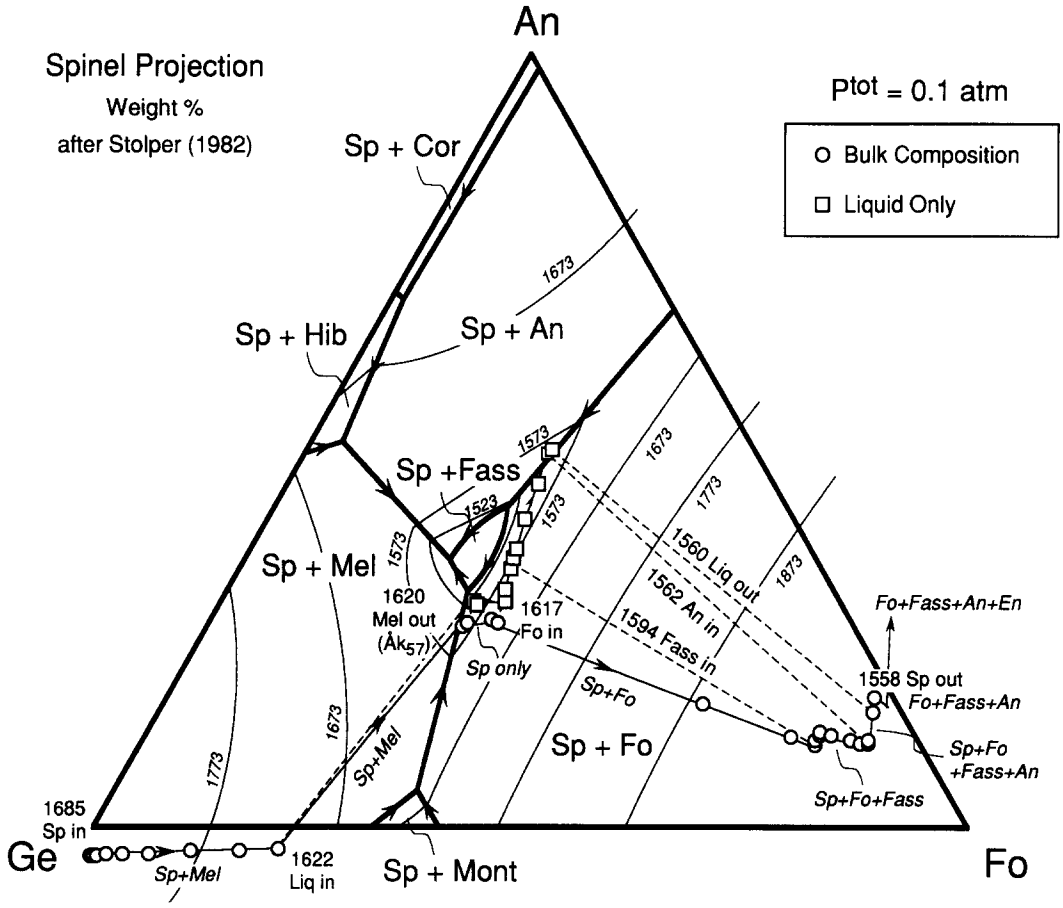

FIG. 17. Calculated composition-temperature trajectories of bulk condensates and their liquid fractions at $P^{tot} = 0.1$ atm superimposed upon the crystal-liquid phase relations in a portion of the CMAS system projected from $MgAl_2O_4$ spinel onto the gehlenite-anorthite-forsterite plane. Abbreviations and conventions as used previously.

librium assemblage of forsterite + anorthite + liquid. Under these circumstances, the calculated liquid composition at this temperature should lie on the forsterite-anorthite-spinel boundary curve but plots instead just to the wollastonite-rich side of it. Between 1587 and 1540 K, the calculated equilibrium assemblage is forsterite + anorthite + liquid and, accordingly, all liquid compositions plot within the forsterite + anorthite field and have calculated equilibration temperatures quite compatible with the observed isotherms. At 1540 K, anorthite is predicted to be consumed and it is indeed quite conceivable that the liquid composition calculated for this temperature lies above the observed 1540 K isotherm. At 1536 K, enstatite is predicted to become stable and the liquid composition indeed crosses into the forsterite + protoenstatite field. At 1532 K, anorthite is calculated to become stable again, and the phase diagram shows that this is due to the fact that so much enstatite has crystallized from the liquid that the liquid composition has migrated back to the forsterite-protoenstatite-anorthite cotectic. At 1523 K, fassaite is calculated to become stable as the liquid disappears. This is only 6 K above the temperature of the quaternary invariant point, 1517 K (Libourel et al., 1989), at which diopsidic pyroxene is one of the crystallizing phases (Fig. 20), and the calculated composition of the final liquid plots just slightly to the An-rich side of that point.

In summary, the compositions of condensate liquids calculated to be in equilibrium with condensate mineral assemblages are in excellent agreement with the topologies of experimentally determined liquid-crystal phase diagrams. The calculated equilibration temperatures are also in excellent agreement with those observed experimentally, except when condensation calculations predict intermediate members of solid solution series, such as melilite and fassaite, to be in equilibrium with liquids. The latter discrepancies are due to the previously discussed limitation of the Berman (1983) liquid model, i.e., the thermodynamic properties of the liquid are never constrained by the solution properties of intermediate members of solid solution series. The ~100 K discrepancies between calculated and observed equilibration temperatures of liquid and melilite (Figs. 18, 19) are due to the fact that the calculations predict that the melilite in question has the composition $Åk_{39}$ at $P^{tot} = 0.3$ atm and $Åk_{57}$ at $P^{tot} = 0.1$ atm, while the thermodynamic model for the liquid has only been "taught" the thermodynamic properties of pure gehlenite and pure åkermanite. Similarly, the 50–80 K discrepancies between calculated and observed equilibration temperatures of liquid and fassaite (Fig. 19) are due to the fact that the calculated fassaite contains ~16 mol% CaTs, 2.3–6.9 mol% T_3P, and 4–17 mol% T_4P, while the only Ca-rich

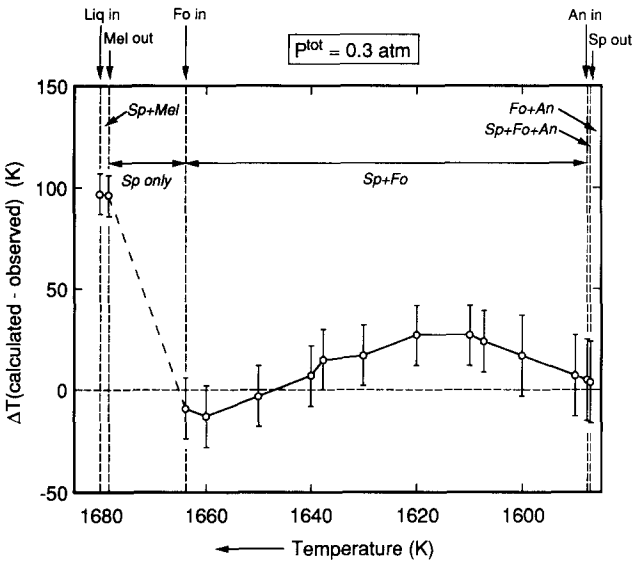

FIG. 18. Difference between calculated liquid-crystal equilibration temperature at P^{tot} = 0.3 atm and the experimentally observed temperature of equilibration of a liquid of the same composition and the same solid phase assemblage plotted against calculated temperatures along the liquid composition trajectory in Fig. 16. Vertical lines mark events labelled on the trajectory and separate segments labelled by the mineral assemblages calculated to be in equilibrium with liquids over the temperature intervals of the segments. Error bars are estimates of uncertainties in the observed temperatures due to interpolating between isotherms. Abbreviations as used previously.

pyroxene composition whose thermodynamic data constrain the liquid model is pure diopside. It is noteworthy that, in the case of both solid solution phases, these errors cause us to overestimate crystal-liquid equilibration temperatures. This is particularly important because the liquid which persists to the lowest P^{tot}, 5×10^{-2} atm (Fig. 5), and to the lowest dust/gas ratio, 16 (Fig. 12), is simultaneously in equilibrium with both of these solid solution phases, in addition to spinel and forsterite. It is thus the solidus temperature of this liquid, 1508 K (Treiman, 1990), which determines the minimum total pressure or dust/gas ratio necessary to stabilize liquid condensates. Our calculations overestimate the temperature of complete crystallization of this liquid by ~50 K at $P^{tot} = 5 \times 10^{-2}$ atm and also at a dust/gas ratio enhancement of 16 at $P^{tot} = 1 \times 10^{-3}$ atm. This suggests that it may be necessary to revise downward our estimate of the minimum total pressure for stabilizing liquids in a solar gas to $\sim 1 \times 10^{-2}$ atm, remarkably similar to the estimate of 5.6×10^{-3} atm by Grossman and Clark (1973). Similarly, the minimum dust/gas enrichment factor necessary for stabilizing liquids at $P^{tot} = 1 \times 10^{-3}$ atm could be as low as only 5 relative to the solar abundances. The implication is very clear. For the past 25 years, theoretical investigations of the condensation of solids from a solar gas at $P^{tot} = 1 \times 10^{-3}$ atm and no enhancement in the dust/gas ratio were actually carried out under conditions which were perched on the edge of the liquid stability field, at least as far as CaO-, Al_2O_3-rich compositions are concerned.

7. APPLICATION TO SOME PHASE ASSEMBLAGES IN CHONDRITES

7.1. Types A, B, and C Refractory Inclusions

Refractory, Ca-, Al-rich inclusions in Allende and other C3 chondrites fall into four main groups on the basis of their mineralogical compositions. Fluffy Type A inclusions are composed of major amounts of melilite and spinel, and minor perovskite and hibonite, and were probably never molten. Compact Type A inclusions contain major amounts of melilite and spinel and accessory perovskite, and may contain minor fassaite and/or rhönite [$Ca(Ca, Mg, Al, Ti)_3(Si, Al)_3O_{10}$], and were probably at least partially molten. Type B inclusions contain major amounts of melilite, spinel, fassaite, and minor anorthite, and were certainly molten. Type C inclusions contain the same minerals as Type Bs but anorthite is the major phase in the former, comprising 30–60 vol%. Type C inclusions crystallized from melts.

Bulk chemical compositions of individual Types A and B inclusions from Sylvester et al. (1993) and of Type C inclusions from Wark (1987) are plotted in Figs. 21 and 22, the same spinel projection onto the gehlenite-anorthite-forsterite plane seen in Figs. 16 and 17. Included are data for inclusions from the reduced subgroup of CV3s measured by Sylvester et al. (1993) or compiled from literature sources by them, and for Allende inclusions corrected for secondary alteration effects in the literature sources cited by Sylvester et al. (1993). Also plotted are the composition trajectories of bulk condensates and the liquid fractions thereof calculated at several different total pressures (Fig. 21) and several different dust/gas ratio enhancements at $P^{tot} = 1 \times 10^{-3}$ atm (Fig. 22). Note how closely two of the calculated trajectories, those for P^{tot} = 0.3 atm and for a dust/gas ratio enhancement of 40 relative to solar abundances at a total pressure of 1×10^{-3} atm, pass through the trends for both Type A and Type B inclusions in

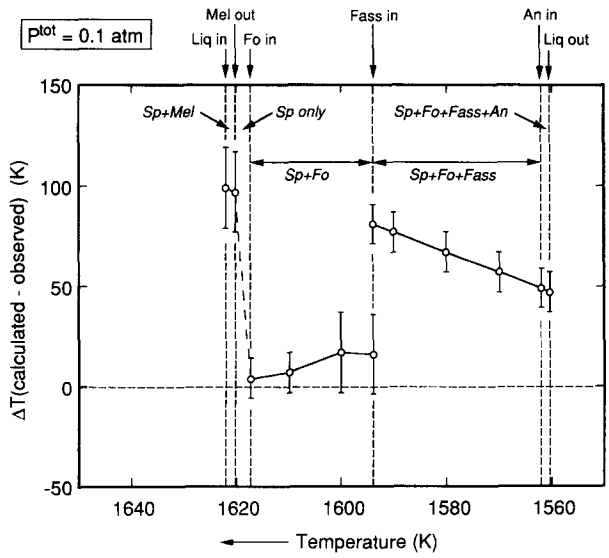

FIG. 19. Difference between calculated liquid-crystal equilibration temperature at P^{tot} = 0.1 atm and the experimentally observed temperature of equilibration of a liquid of the same composition and the same solid phase assemblage plotted against calculated temperatures along the liquid composition trajectory in Fig. 17.

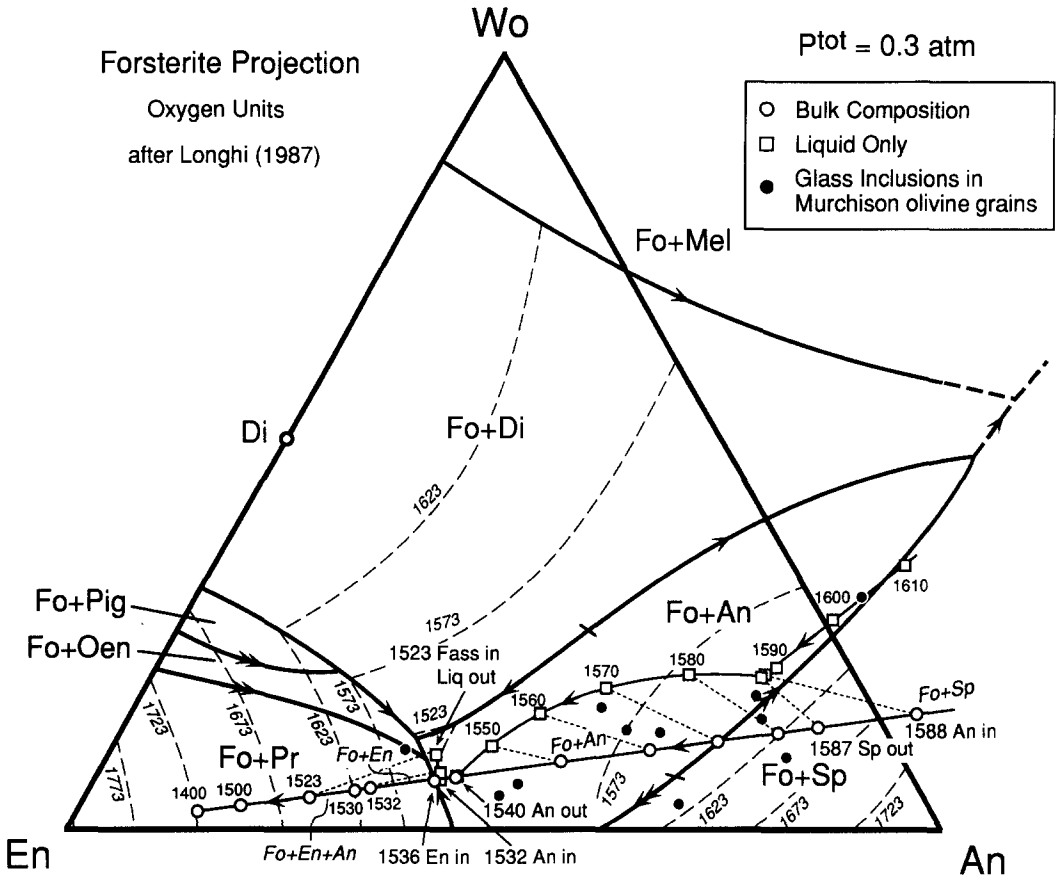

FIG. 20. Calculated composition-temperature trajectories of bulk condensates and their liquid fractions at $P^{tot} = 0.3$ atm superimposed upon the crystal-liquid phase relations in a portion of the CMAS system projected from forsterite onto the enstatite-anorthite-wollastonite plane. Also plotted are compositions of glass inclusions in Murchison forsterite grains. Wo, wollastonite; Oen, orthoenstatite; Pr, protoenstatite; Pig, pigeonite [$(Ca, Mg)_2Si_2O_6$]. Other abbreviations and conventions as used previously.

this projection. Note also that none of the trajectories fall close to the compositions of Type C inclusions. Along the segment of the bulk composition trajectory which passes through the compositions of Type A inclusions, the equilibrium condensate assemblage is spinel + melilite + perovskite. At 0.3 atm total pressure, melilite and spinel in this assemblage begin to react with gaseous Si and Mg at 1680 K to form a liquid which is much richer in MgO and SiO_2 than the starting composition (Fig. 3). Perovskite might be able to dissolve in the liquid at this temperature but our use of the Berman (1983) liquid model does not allow us to calculate the distribution of Ti between solid and liquid phases. Melilite dissolves completely in this liquid by 1678 K, causing the composition of the liquid to migrate across the spinel + melilite field, carrying the composition of the bulk condensate along with it (Fig. 16). This is the cause of the abrupt departure of these trajectories from the horizontal segment through the Type A inclusion compositions on Fig. 21 and the passage of these trajectories directly through the middle of the field of Type B inclusion compositions. If this assemblage continues to equilibrate with the gas, Mg and Si will continue to condense into the liquid, causing the composition of both it and the bulk condensate to migrate horizontally across the melilite-forsterite boundary curve in Figs. 16 and 21. If, instead, complete dissolution of melilite in the liquid is followed by isolation of the condensate from further reaction with the gas, then, upon cooling, melilite and spinel will crystallize from the liquid, driving the residual liquid composition towards the fassaite and anorthite fields where both of these phases will crystallize. The result would be an assemblage with both the chemical and mineralogical composition of a Type B inclusion. In other words, formation of Type B inclusions could be the natural consequence of the reaction of a solid assemblage having the chemical and mineralogical composition of a Type A inclusion with the gas to produce a liquid during condensation, either in a solar gas at 0.3 atm total pressure or at 1×10^{-3} atm in a system whose composition has been enriched in dust relative to gas by a factor of ~40 compared to solar abundances. The same reaction is possible at lower total pressures but only if the dust/gas ratio enhancement were greater than that needed at 1×10^{-3} atm. Failure of the calculated trajectories to pass through the compositions of Type C inclusions implies that the latter did not form in a simple process involving direct, equilibrium condensation over the total pressure range 0.1 to 1 atm or at dust/gas enrichment factors of 40 to 70 at 1×10^{-3} atm, contrary to the conclusion of Wark (1987).

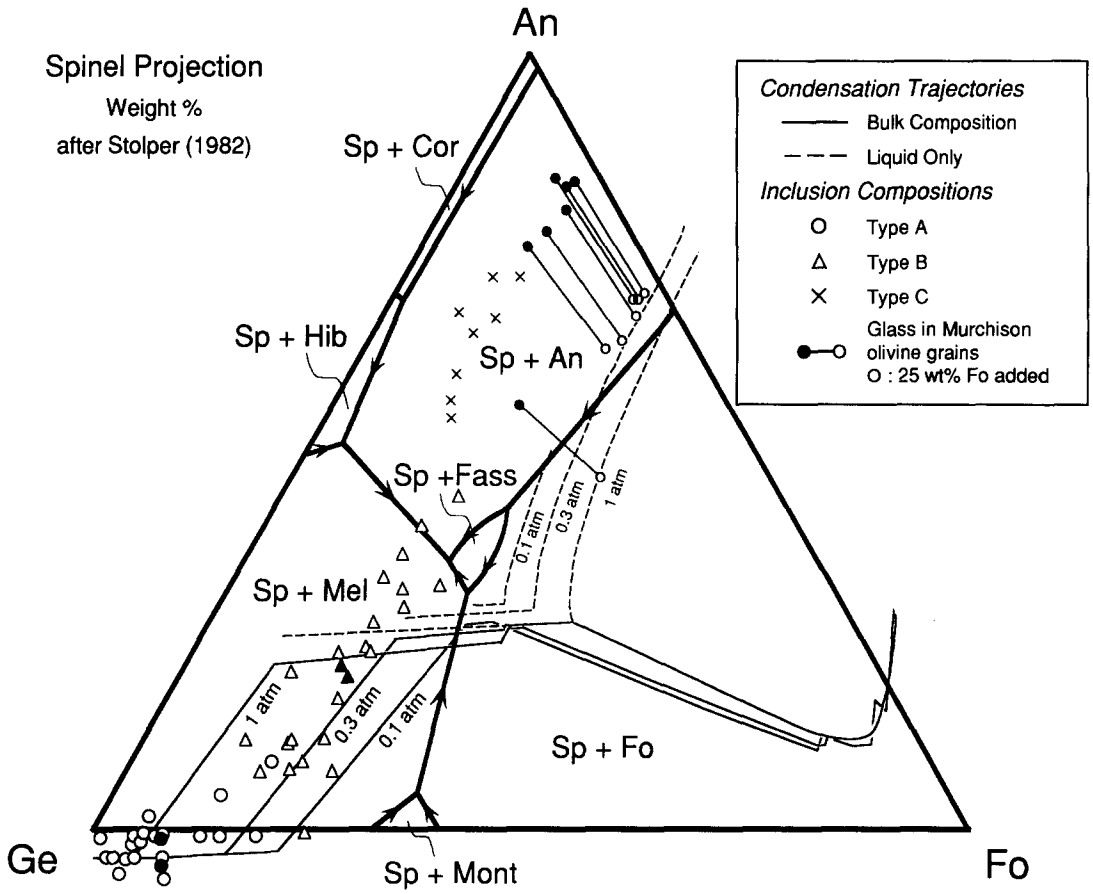

FIG. 21. Calculated composition trajectories of bulk condensates and their liquid fractions at several different total pressures projected onto the same phase diagram as in Fig. 16. Also plotted are bulk compositions of individual Types A, B, and C refractory inclusions in CV3 chondrites and of glass inclusions in isolated forsterite crystals in the Murchison CM2 chondrite. Large, filled circles, and filled triangles are average compositions of Type A and Type B inclusions, respectively, one of each estimated from Allende inclusions corrected for secondary alteration effects and the other from inclusions from the reduced subgroup of CV3 chondrites. Each small, filled circle representing the composition of a glass inclusion is connected by a straight line to a small, open circle representing the composition of the same inclusion to which 25 wt% forsterite has been added. Abbreviations and conventions as used previously.

It should be pointed out here that projection of compositions from spinel, as in Figs. 21 and 22, masks real differences in CaO/Al_2O_3 ratios between measured and calculated compositions. As first noted by Beckett (1986) and confirmed by Sylvester et al. (1993), most Types A and B inclusions have superchondritic CaO/Al_2O_3 ratios which cannot be understood in terms of simple, subsolidus condensation calculations, as the latter predict refractory inclusion-like compositions only after both Al_2O_3 and CaO are fully condensed. Nor can they be understood in terms of the liquid condensation models presented herein for exactly the same reason. The explanation proposed by Beckett (1986) and Sylvester et al. (1993) was that condensation of Types A and B inclusions occurred after removal of higher-temperature, Al_2O_3-rich condensates. Another possibility is undersampling of spinel by inclusion precursors due to some physical process in the solar nebula which caused fractionation of this phase. Although simple addition of spinel to Type A inclusions would bring the compositions of virtually all of them into complete agreement with condensate compositions, it is more difficult to see if such an effect can explain Type B inclusion compositions. This is because the measured compositions of Type B inclusions all suffer from laboratory bias related to the nonrepresentativeness of sampling small portions of relatively coarse-grained inclusions and to the difficulty of sampling the proper core/mantle proportions in radially zoned Type B1s.

Note that, if the above model for production of Type B inclusion melts is correct, the relatively rapid cooling rates for the latter, 1–50°C/h, deduced by MacPherson et al. (1984) become a serious constraint on the condensation process itself. MacPherson et al. (1984) dismissed the fact that these cooling rates are much faster than would be reasonable for the cooling rate of the solar nebula by proposing that solid assemblages that had condensed in a slowly cooled nebula were later heated to melting in a localized region by some transient source and then solidified upon cooling at a rate comparable to that of the local region. In the present model, however, melting is an integral part of the condensation process, and the heat source for production of melt is the same as the one that vaporized the dust. Rejecting the notion that the MacPherson et al. (1984) cooling rates were characteristic of vast regions of the nebular cloud implies either that refrac-

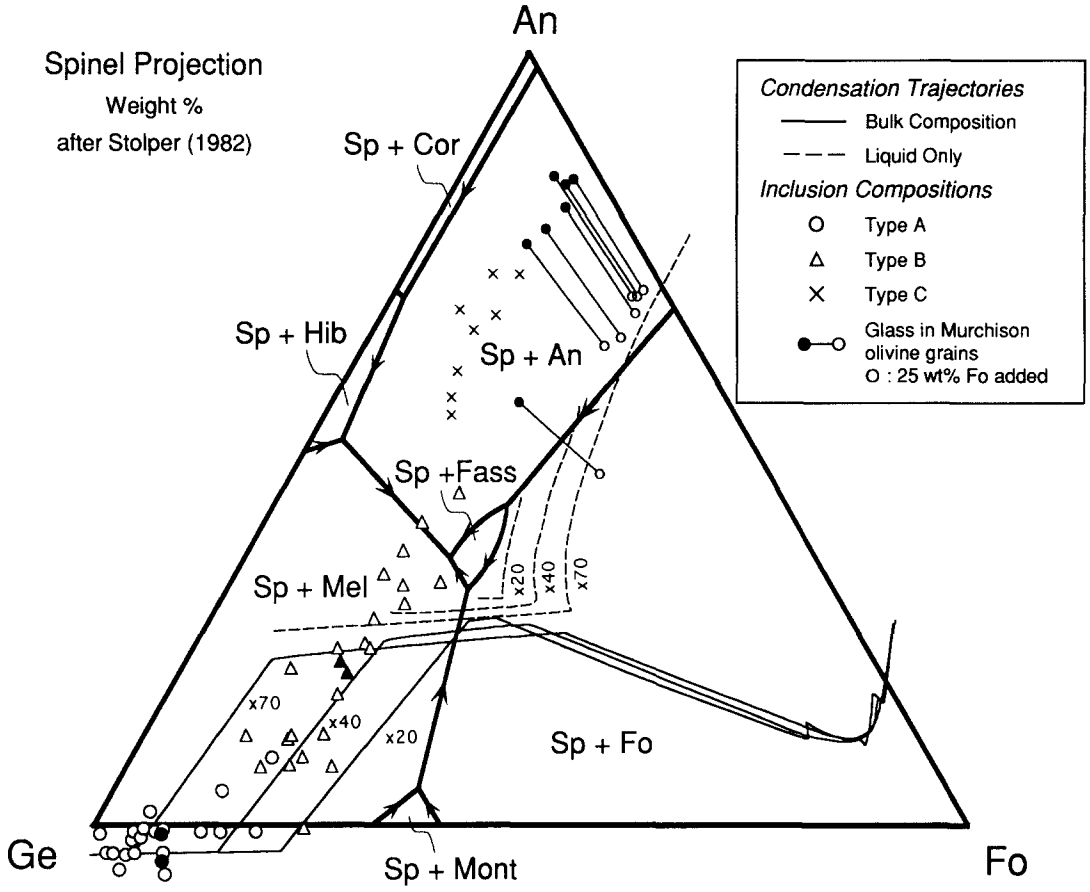

FIG. 22. Calculated composition trajectories of bulk condensates and their liquid fractions at several different dust/gas enrichment factors relative to solar abundances at $P^{tot} = 1 \times 10^{-3}$ atm projected onto the same phase diagram as in Fig. 16. Abbreviations, conventions and symbols as in Fig. 21.

tory inclusions condensed in a locally heated region or that, once the partial melt droplets formed during condensation in a slowly cooled region, they were quickly removed to a cooler region, perhaps by the same process that prevented them from further chemical equilibration with the vapor, where they cooled at 1–50°C/h.

Note also that there is no opportunity in this model to develop the oxygen isotopic heterogeneity observed among the major phases of Type B inclusions (Clayton et al., 1977). One could imagine that condensation began from a gas enriched in ^{16}O. If the surrounding gas had become less ^{16}O-rich by the time the liquid formed, the remaining spinel might have been able to retain its low $\delta^{18}O$ and $\delta^{17}O$ values while the liquid underwent oxygen isotopic exchange with the gas. Recall that production of Type B inclusions requires that there be no further chemical interaction of the melt droplets with the gas beyond this stage in order to prevent massive addition of forsterite to the condensate assemblage. Cooling of these Type B melt droplets results in crystallization of melilite, fassaite, anorthite, and more spinel. Because melilite and fassaite co-crystallize from the same liquid, fassaite would have the same $\delta^{18}O$ as melilite, higher than that of the spinel. Thus, although such a sequence of events could possibly explain why spinel has a lower $\delta^{18}O$ than the other phases of Type B inclusions, it cannot explain why fassaite is observed to have a lower $\delta^{18}O$ value than melilite, similar to that of the spinel. This problem was also encountered by Clayton et al. (1977) who proposed a similar model. Thus, even if Type B inclusions formed as suggested herein, the oxygen isotopic heterogeneity observed among their constituent minerals must still be ascribed to differential isotopic exchange of ^{16}O-rich solid phases with a more isotopically normal gas after the liquid stage, as was originally suggested by Blander and Fuchs (1975).

7.2. Glass Inclusions in Isolated Forsterite Crystals in CM2 Chondrites

Murchison and other CM2 chondrites contain large forsterite crystals which Grossman and Olsen (1974) interpreted as high-temperature, nebular condensates on the basis of their euhedral nature, textural setting, low FeO contents, and the compositions of their included metallic nickel-iron grains. In contrast, Richardson and McSween (1978) considered the forsterite grains to be crystallization products of chondrule melts, an argument refuted on textural and chemical grounds by Olsen and Grossman (1978). These forsterite grains have ovate inclusions of glass, up to 36 μm in size, normally containing 15–20% CaO, 2–7% MgO, 20–28% Al_2O_3, and 45–55% SiO_2 (Fuchs et al., 1973). The presence of these glass

inclusions was difficult to reconcile with the proposed condensation origin of their host forsterite grains because, up until that time, stable liquids were predicted by condensation models to be in equilibrium with forsterite in a solar gas only at total pressures greater than 100 atm (Wood, 1963), far higher than the maximum pressures allowed by hydrodynamic models of the solar nebula. It is worth re-examining the origin of these glass inclusions in light of the models presented herein, in which CMAS condensate liquids are predicted to be in equilibrium with forsterite at much lower total pressures than this, with or without dust/gas enrichment.

Three of the fourteen glass inclusions analysed by Fuchs et al. (1973) have relatively high concentrations of FeO (>2%) and Na_2O (up to 1.8%) which may be due to secondary alteration. Compositions of all remaining inclusions are plotted on the forsterite projection in Fig. 20, in which they fall within or close to the boundary of the forsterite + anorthite field and scatter about the composition trajectory for the total condensate at $P^{tot} = 0.3$ atm, which is identical to that calculated for a dust/gas enrichment factor of 70 at $P^{tot} = 1 \times 10^{-3}$ atm. From 1587 to 1540 K at $P^{tot} = 0.3$ atm, the equilibrium condensate assemblage is forsterite + anorthite + liquid. Note that, if anorthite failed to nucleate from the condensate liquid, the composition of the liquid would be coincident with that of the bulk condensate in this projection. When projected from spinel, seven of the inclusions fall within the gehlenite-forsterite-anorthite triangle and, in particular, inside the spinel + anorthite field. Projected in this way, their compositions are compared to the composition trajectories of the total condensates and their liquid fractions at several different total pressures in Fig. 21 and at different dust/gas enrichment factors at $P^{tot} = 1 \times 10^{-3}$ atm in Fig. 22. None of the calculated trajectories pass through the glass compositions. If it is assumed, however, that, after liquid droplets were trapped by the growing forsterite crystals, the compositions of the droplets were modified by precipitation of 25% forsterite as a daughter mineral, corresponding to only a 2–3 μm thick layer of forsterite surrounding each of the inclusions, the corrected compositions shown on Figs. 21 and 22 would result. Note that the condensate liquid composition trajectories calculated for $P^{tot} = 0.3$ atm in Fig. 21 and for a dust/gas enrichment factor of 70 at $P^{tot} = 1 \times 10^{-3}$ atm in Fig. 22 pass through the corrected glass compositions. Furthermore, these condensate liquid trajectories are virtually unchanged if anorthite precipitation is suppressed. The reason why the necessity for the forsterite correction is not apparent in Fig. 20 is that the compositions in that figure are projected from forsterite, causing each original composition and its forsterite-corrected counterpart to be coincident. It is concluded that, if the original liquid compositions were modified in the way suggested here, the glass inclusions represent droplets of liquid which may indeed have been in equilibrium with their host forsterite crystals during nebular condensation. As in the case of Type B inclusions, however, the original forsterite + liquid assemblage had to be isolated from further reaction with the gas in order to prevent wholesale conversion of forsterite to enstatite and also had to be cooled quickly in order to prevent nucleation of anorthite and to quench the liquid to a glass. Note that kinetic suppression of anorthite nucleation would be unnecessary for $P^{tot} \geq 1$ atm and for dust/gas enrichment factors ≥ 100 at $P^{tot} = 1 \times 10^{-3}$ atm because, under these conditions, condensation occurs at such a high temperature that anorthite does not crystallize from the liquid, and the equilibrium assemblage is thus forsterite plus a liquid whose composition trajectory passes as close to the glass inclusion compositions as those in Figs. 21 and 22.

7.3. Chondrules

Ever since Wood (1963) showed that forsterite could not be in equilibrium with a melt of its own composition in a solar gas unless the total pressure exceeded 100 atm, it has been assumed that liquid precursors of chondrules could not have formed as equilibrium condensates because such pressures are much higher than those predicted in virtually all hydrodynamic models of the evolution of the solar nebula. The calculations presented herein show significant temperature intervals for the stable coexistence of forsterite + liquid in a solar gas at total pressures as low as 5×10^{-2} atm and at even lower pressures in cosmic gases made from dust-enriched systems. The much lower minimum P^{tot} for stabilizing forsterite + liquid condensate assemblages in a solar gas in this work than in the work of Wood (1963) is due to the colligative effects of additional components, in this case CaO and Al_2O_3, which were not considered by Wood (1963). The possibility that this might be the case was theorized by Wagner and Larimer (1978). Our calculations suggest that the question of whether chondrules are liquid condensates that formed at equilibrium in either a solar gas or in a cosmic gas made from a dust-enriched system should be reopened. In order for this question to be properly addressed, however, thermodynamic models for liquids, such as the Berman (1983) model used herein, will have to be extended to include additional components which are important in refractory inclusions and chondrules, such as TiO_2, Ti_2O_3, FeO, and Na_2O, and will have to be constrained by the thermodynamic properties of intermediate members of solid solution series, such as melilite, fassaite, olivine, low-Ca pyroxene, and plagioclase. Extension of liquid models to include FeO and Na_2O are likely to produce lower solidus temperatures, and may allow condensate melts to persist to lower temperature, requiring even lower minimum total pressures to stabilize melts of chondrule compositions. The abundant textural evidence for rapid crystallization of chondrule melts implies, if partial melts of chondrule compositions can be produced during condensation, that at least the stage in the process during which the last melt solidifies must be a period of rapid cooling.

8. CONCLUSIONS

1) Incorporation of the Berman (1983) activity-composition model for CMAS liquids into condensation calculations results in predicted crystal + liquid assemblages which are in excellent agreement with the topology of experimentally determined, crystal-liquid phase diagrams and in predicted crystal-liquid equilibration temperatures which are in excellent agreement with measured ones, except where intermediate members of solid solution series, such as melilite and fassaite, are in equilibrium with liquid, in

which cases equilibration temperatures are overestimated by 50 to 100 K.

2) Predicted condensate liquids are very non-ideal, suggesting that results of attempts to model their formation using ideal solution approximations (Bartholomay and Larimer, 1982; Larimer and Bartholomay, 1983; Wood and Hashimoto, 1993) are highly inaccurate.
3) CMAS liquids are stable in a solar gas at a minimum P^{tot} of 5×10^{-2} atm and perhaps as low as 1×10^{-2} atm, quite close to the estimate by Grossman and Clark (1973) of 5.6×10^{-3} atm.
4) CMAS liquids are stable at lower P^{tot} in gases made by vaporization of systems enriched in dust relative to gas compared to the solar abundances, e.g., at 1×10^{-3} atm for a dust/gas enrichment factor at least as low as 16 and perhaps as low as 5 relative to solar abundances, and at even lower P^{tot} at higher minimum dust/gas enhancements.
5) Forsterite is in equilibrium with condensate liquids over wide ranges of P^{tot} and dust/gas enrichment factor, including the lowest-temperature liquids which appear at the lowest P^{tot} in (3) and lowest dust/gas enhancements in (4). The minimum P^{tot} for stable coexistence of forsterite + liquid in a solar gas is thus several orders of magnitude lower than that estimated by Wood (1963) due to the colligative effects of CaO and Al_2O_3 which were not considered by Wood.
6) Type B inclusions may have formed when a crystalline Type A mineral assemblage reacted with the gas upon cooling to yield a partial melt which was much richer in MgO and SiO_2 than the starting material and which solidified after being isolated from further reaction with the gas, either in a solar gas at $P^{tot} \sim 0.3$ atm or in a system whose dust/gas enrichment factor was ~40 at $P^{tot} = 1 \times 10^{-3}$ atm.
7) Glass inclusions in the large, isolated forsterite crystals in the Murchison CM2 chondrite may be derived from condensate liquids which formed in a solar gas at $P^{tot} = 0.3$ atm or in a system whose dust/gas enrichment factor was ~70 at $P^{tot} = 1 \times 10^{-3}$ atm.

Acknowledgments—We thank E. Stolper and J. R. Beckett for the idea of incorporating the Berman liquid activity model into our condensation program and for assisting us in doing so. We also thank J. R. Beckett for helping us estimate the free energies of the Ti-bearing pyroxene components, R. C. Newton for helping us select and use thermodynamic data, A. M. Davis for computer drawings of phase diagrams, and S. B. Simon for helpful discussions. Funding from the National Aeronautics and Space Administration through grant NAGW-3340 is gratefully acknowledged.

Editorial handling: R. A. Schmitt

REFERENCES

Allibert M., Chatillon C., Jacob K. T., and Lourtau R. (1981) Mass-spectrometric and electrochemical studies of thermodynamic properties of liquid and solid phases in the system $CaO-Al_2O_3$. *J. Amer. Ceram. Soc.* **64,** 307–314.

Anders E. and Grevesse N. (1989) Abundances of the elements: Meteoritic and solar. *Geochim. Cosmochim. Acta* **53,** 197–214.

Barin I. (1989) *Thermochemical Data of Pure Substances, Part I.* VCH, Weinheim, Germany.

Barron L. M. (1985) Comment on "A thermodynamic model for multicomponent melts, with application to the system $CaO-Al_2O_3-SiO_2$" by R. G. Berman and T. H. Brown. *Geochim. Cosmochim. Acta* **49,** 611–612.

Barron L. M. (1986) Some thermodynamic properties of the Berman and Brown model for $CaO-Al_2O_3-SiO_2$. *Geochim. Cosmochim. Acta* **50,** 2727–2733.

Bartholomay H. A. and Larimer J. W. (1982) Dust-gas fractionation in the early solar system. *Meteoritics* **17,** 180–181 (abstr.).

Beckett J. R. (1986) The origin of calcium-, aluminum-rich inclusions from carbonaceous chondrites: an experimental study. Ph.D. thesis, Univ. Chicago.

Berman R. G. (1983) A thermodynamic model for multicomponent melts, with application to the system $CaO-MgO-Al_2O_3-SiO_2$. Ph.D. thesis, Univ. British Columbia.

Berman R. G. and Brown T. H. (1985) Heat capacity of minerals in the system $Na_2O-K_2O-CaO-MgO-FeO-Fe_2O_3-Al_2O_3-SiO_2-TiO_2-H_2O-CO_2$: representation, estimation, and high temperature extrapolation. *Contrib. Mineral. Petrol.* **89,** 168–183.

Blander M. and Fuchs L. H. (1975) Calcium- aluminum-rich inclusions in the Allende meteorite: evidence for a liquid origin. *Geochim. Cosmochim. Acta* **39,** 1605–1619.

Blander M. and Pelton A. D. (1987) Thermodynamic analysis of binary liquid silicates and prediction of ternary solution properties by modified quasichemical equations. *Geochim. Cosmochim. Acta* **51,** 85–95.

Cameron A. G. W. (1973) Abundances of the elements in the solar system. *Space Sci. Revs.* **15,** 121–146.

Chamberlin L., Beckett J. R., and Stolper E. M. (1992) Experimental determination of oxide activities in synthetic CAI and POI melts. *Lunar Planet. Sci. XXIII,* 215–216 (abstr.).

Chamberlin L., Beckett J. R., and Stolper E. (1994) Pd-oxide equilibration: a new experimental method for the direct determination of oxide activities in melts and minerals. *Contrib. Mineral. Petrol.* **116,** 169–181.

Chamberlin L., Beckett J. R., and Stolper E. M. (1995a) Palladium oxide equilibration and the thermodynamic properties of $MgAl_2O_4$ spinel. *Amer. Mineral.* **80,** 285–296.

Chamberlin L., Beckett J. R., and Stolper E. M. (1995b) Experimental measurement of oxide activities across the join $MgAl_2O_4-Al_{8/3}O_4$ at 1400°C. *Amer. Mineral.* (submitted).

Charlu T. V., Newton R. C., and Kleppa O. J. (1978) Enthalpy of formation of some lime silicates by high-temperature solution calorimetry, with discussion of high pressure phase equilibria. *Geochim. Cosmochim. Acta* **42,** 367–375.

Charlu T. V., Newton R. C., and Kleppa O. J. (1981) Thermochemistry of synthetic $Ca_2Al_2SiO_7$ (gehlenite)-$Ca_2MgSi_2O_7$ (åkermanite) melilites. *Geochim. Cosmochim. Acta* **45,** 1609–1617.

Clayton R. N., Onuma N., Grossman L., and Mayeda T. K. (1977) Distribution of the presolar component in Allende and other carbonaceous chondrites. *Earth Planet. Sci. Lett.* **34,** 209–224.

De Capitani C. and Brown T. H. (1987) The computation of chemical equilibrium in complex systems containing non-ideal solutions. *Geochim. Cosmochim. Acta* **51,** 2639–2652.

Fegley M. B., Jr. (1981) The thermodynamic properties of silicon oxynitride. *J. Amer. Ceram. Soc.* **64,** C124–C126.

Fegley M. B., Jr. and Palme H. (1985) Evidence for oxidizing conditions in the solar nebula from Mo and W depletions in refractory inclusions in carbonaceous chondrites. *Earth Planet. Sci. Lett.* **72,** 311–326.

Fuchs L. H., Olsen E., and Jensen K. J. (1973) Mineralogy, mineral-chemistry, and composition of the Murchison (C2) meteorite. *Smithsonian Contrib. Earth Sci.* **10.**

Geiger C. A., Kleppa O. J., Mysen B. O., Lattimer J. M., and Grossman L. (1988) Enthalpies of formation of $CaAl_4O_7$ and $CaAl_{12}O_{19}$ (hibonite) by high temperature, alkali borate solution calorimetry. *Geochim. Cosmochim. Acta* **52,** 1729–1736.

Ghiorso M. S., Carmichael I. S. E., Rivers M. L., and Sack R. O. (1983) The Gibbs Free Energy of mixing of natural silicate liquids; an expanded regular solution approximation for the calculation of magmatic intensive variables. *Contrib. Mineral. Petrol.* **84,** 107–145.

Grossman L. (1972) Condensation in the primitive solar nebula. *Geochim. Cosmochim. Acta* **36,** 597–619.

Grossman L. and Clark S. P., Jr. (1973) High-temperature condensates in chondrites and the environment in which they formed. *Geochim. Cosmochim. Acta* **37,** 635–649.

Grossman L. and Olsen E. (1974) Origin of the high-temperature fraction of C2 chondrites. *Geochim. Cosmochim. Acta* **38,** 173–187.

Grossman L., Olsen E., and Lattimer J. M. (1979) Silicon in carbonaceous chondrite metal: Relic of high-temperature condensation. *Science* **206,** 449–451.

Holland T. J. B. (1989) Dependence of entropy on volume for silicate and oxide minerals: A review and predictive model. *Amer. Mineral.* **74,** 5–13.

JANAF (1985) Thermochemical Tables. 3rd ed. (ed. M. W. Chase Jr. et al.). *J. Phys. Chem. Ref. Data* **14** (Suppl. 1).

Krot A., Ivanova M. A., and Wasson J. T. (1993) The origin of chromitic chondrules and the volatility of Cr under a range of nebular conditions. *Earth Planet. Sci. Lett.* **119,** 569–584.

Larimer J. W. and Bartholomay H. A. (1983) Gas-dust fractionation and the origin of chondritic meteorites. *Lunar Planet. Sci. XIV,* 423 (abstr.).

Lattimer J. M., Schramm D. N., and Grossman L. (1978) Condensation in supernova ejecta and isotopic anomalies in meteorites. *Astrophys. J.* **219,** 230–249.

Libourel G., Boivin P., and Biggar G. M. (1989) The univariant curve liquid = forsterite + anorthite + diopside in the system CMAS at 1 bar: solid solutions and melt structure. *Contrib. Mineral. Petrol.* **102,** 406–421.

Longhi J. (1987) Liquidus equilibria and solid solution in the system $CaAl_2Si_2O_8$–Mg_2SiO_4–$CaSiO_3$–SiO_2 at low pressure. *Amer. J. Sci.* **287,** 265–331.

MacPherson G. J., Paque J. M., Stolper E., and Grossman L. (1984) The origin and significance of reverse zoning in melilite from Allende Type B inclusions. *J. Geol.* **92,** 289–305.

Muan A. and Osborn E. F. (1965) *Phase Equilibria among Oxides in Steelmaking.* Addison-Wesley.

Newton R. C., Charlu T. V., and Kleppa O. J. (1980) Thermochemistry of the high structural state plagioclases. *Geochim. Cosmochim. Acta* **44,** 933–941.

Nurse R. W., Welch J. H., and Majumdar A. J. (1965) The CaO–Al_2O_3 system in a moisture-free atmosphere. *Trans. Brit. Cer. Soc.* **64,** 409–418.

Olsen E. and Grossman L. (1978) On the origin of isolated olivine grains in Type 2 carbonaceous chondrites. *Earth Planet. Sci. Lett.* **41,** 111–127.

Onuma K. and Kimura M. (1978) Study of the system $CaMgSi_2O_6$–$CaFe^{3+}AlSiO_6$–$CaAl_2SiO_6$–$CaTiAl_2O_6$: II. The join $CaMgSi_2O_6$–$CaAl_2SiO_6$–$CaTiAl_2O_6$ and its bearing on Ca-Al-rich inclusions in carbonaceous chondrite. *J. Fac. Sci. Hokkaido Univ., Ser. IV* **18,** 215–236.

Press W. H., Teukolsky S. A., Vetterling W. T., and Flannery B. P. (1992) *Numerical Recipes in FORTRAN. The Art of Scientific Computing.* 2nd ed. Cambridge Univ. Press.

Rein R. H. and Chipman J. (1965) Activities in the liquid solution SiO_2–CaO–MgO–Al_2O_3 at 1600°C. *Trans. Met. Soc. AIME* **233,** 415–425.

Richardson S. M. and McSween H. Y., Jr. (1978) Textural evidence bearing on the origin of isolated olivine crystals in C2 carbonaceous chondrites. *Earth Planet. Sci. Lett.* **37,** 485–491.

Richet P., Robie R. A., and Hemingway B. S. (1991) Thermodynamic properties of wollastonite, pseudowollastonite and $CaSiO_3$ glass and liquid. *European J. Mineral.* **3,** 475–484.

Robie R. A., Hemingway B. S., and Fisher J. R. (1978) *Thermodynamic Properties of Minerals and Related Substances at 298.15 K and 1 Bar (10^5 Pascals) Pressure and at Higher Temperatures; USGS Bull. 1452.*

Robinson G. R., Jr., Haas J. L., Jr., Schafer C. M., and Haselton H. T., Jr. (1982) Thermodynamic and thermophysical properties of selected phases in the MgO–SiO_2–H_2O–CO_2, CaO–Al_2O_3–SiO_2–H_2O–CO_2, and Fe–FeO–Fe_2O_3–SiO_2 chemical systems, with special emphasis on the properties of basalts and their mineral components. *USGS Open-File Report 83-79.*

Rolin M. and Thanh P. H. (1965) Les diagrammes de phases des mélanges ne réagissant pas avec le molybdène. *Rev. Hautes Temp. Refr.* **2,** 175–185.

Sack R. O. (1980) Some constraints on the thermodynamic mixing properties of Fe–Mg orthopyroxenes and olivines. *Contrib. Mineral. Petrol.* **71,** 257–269.

Sack R. O. and Ghiorso M. S. (1991) Chromian spinels as petrogenetic indicators: Thermodynamics and petrological applications. *Amer. Mineral.* **76,** 827–847.

Simon S. B., Grossman L., Podosek F. A., Zinner E., and Prombo C. A. (1994) Petrography, composition, and origin of large, chromian spinels from the Murchison meteorite. *Geochim. Cosmochim. Acta* **58,** 1313–1334.

Smith W. R. and Missen R. W. (1982) *Chemical Reaction Equilibrium Analysis: Theory and Algorithms.* Krieger Publishing Company.

Stolper E. M. (1982) Crystallization sequences of Ca-Al-rich inclusions from Allende: An experimental study. *Geochim. Cosmochim. Acta* **46,** 2159–2180.

Sylvester P. J., Simon S. B., and Grossman L. (1993) Refractory inclusions from the Leoville, Efremovka, and Vigarano C3V chondrites: Major element differences between Types A and B, and extraordinary refractory siderophile element compositions. *Geochim. Cosmochim. Acta* **57,** 3763–3784.

Treiman A. H. (1990) Crystallization of angrites, CAIs and Ca-Al chondrules: Fassaite-spinel liquidi in CMAST. *Lunar Planet. Sci. XXI,* 1262–1263 (abstr.).

Wagner R. and Larimer J. W. (1978) Condensation and stability of chemically heterogeneous substances. *Lunar Planet. Sci. IX,* 1191–1192 (abstr.).

Wark D. A. (1987) Plagioclase-rich inclusions in carbonaceous chondrite meteorites: Liquid condensates? *Geochim. Cosmochim. Acta* **51,** 221–242.

Webb S. A. C. and Wood B. J. (1986) Spinel-pyroxene-garnet relationships and their dependence on Cr/Al ratio. *Contrib. Mineral. Petrol.* **92,** 471–480.

Wood B. J. and Nicholls J. (1978) The thermodynamic properties of reciprocal solid solutions. *Contrib. Mineral. Petrol.* **66,** 389–400.

Wood J. A. (1963) On the origin of chondrules and chondrites. *Icarus* **2,** 152–180.

Wood J. A. (1967) Olivine and pyroxene compositions in Type II carbonaceous chondrites. *Geochim. Cosmochim. Acta* **31,** 2095–2108.

Wood J. A. and Hashimoto A. (1993) Mineral equilibrium in fractionated nebular systems. *Geochim. Cosmochim. Acta* **57,** 2377–2388.

Wood J. A. and McSween H. Y., Jr. (1977) Chondrules as condensation products. In *Comets, Asteroids, Meteorites-Interrelations, Evolution and Origins* (ed. A. H. Delsemme), pp. 365–373. Univ. Toledo.

Yagi K. and Onuma K. (1967) The join $CaMgSi_2O_6$–$CaTiAl_2O_6$ and its bearing on the titanaugites. *J. Fac. Sci. Hokkaido Univ., Ser. IV* **13,** 463–483.

Yang H.-Y. (1976) The join $CaMgSi_2O_6$–$CaAl_2SiO_6$–$CaTiAl_2O_6$ and its bearings on the origin of the Ca- and Al-rich inclusions in the meteorites. *Proc. Geol. Soc. China* **19,** 107–126.

Yang H.-Y., Salmon J. F., and Foster W. R. (1972) Phase equilibria of the join akermanite-anorthite-forsterite in the system CaO–MgO–Al_2O_3–SiO_2 at atmospheric pressure. *Amer. J. Sci.* **272,** 161–188.

Yoneda S. and Grossman L. (1994a) Advanced generation condensation calculations: Compositions of fassaite, spinel and plagioclase in the solar nebula. *Lunar Planet. Sci. XXV,* 1533–1534 (abstr.).

Yoneda S. and Grossman L. (1994b) Calculated stability field and compositions of nonideal condensate liquids in a solar gas. *Meteoritics* **29,** 554–555 (abstr.).

Zhu H., Newton R. C., and Kleppa O. J. (1994) Enthalpy of formation of wollastonite ($CaSiO_3$) and anorthite ($CaAl_2Si_2O_8$) by experimental phase equilibrium measurements and high-temperature solution calorimetry. *Amer. Mineral.* **79,** 134–144.